Atmos. Chem. Phys., 25, 16127–16145, 2025 https://doi.org/10.5194/acp-25-16127-2025 © Author(s) 2025. This work is distributed under the Creative Commons Attribution 4.0 License.





Elemental composition, iron mineralogy, and solubility of anthropogenic and natural mineral dust aerosols in Namibia: a case study analysis from the AEROCLO-sA campaign – Part 2

Paola Formenti¹, Chiara Giorio^{2,3}, Karine Desboeufs¹, Alexander Zherebker², Marco Gaetani⁴, Clarissa Baldo⁵, Gautier Landrot⁶, Simona Montebello^{2,7}, Servanne Chevaillier¹, Sylvain Triquet¹, Guillaume Siour⁵, Claudia Di Biagio¹, Francesco Battaglia¹, Jean-François Doussin⁵, Anais Feron^{1,a}, Andreas Namwoonde⁸, and Stuart John Piketh⁹

¹Université Paris Cité and Univ. Paris Est Creteil, CNRS, LISA, 75013 Paris, France
 ²Yusuf Hamied Department of Chemistry, University of Cambridge, Lensfield Road,
 Cambridge, CB2 1EW, United Kingdom
 ³Dipartimento di Scienze Chimiche, Università degli Studi di Padova, 35131 Padua, Italy
 ⁴Classe di Scienze Tecnologie e Società, Scuola Universitaria Superiore IUSS, 27100, Pavia, Italy

⁴Classe di Scienze Tecnologie e Società, Scuola Universitaria Superiore IUSS, 27100, Pavia, Italy

⁵Univ Paris Est Creteil and Université Paris Cité, CNRS, LISA, 94010 Créteil, France

⁶Synchrotron SOLEIL, L'Orme des Merisiers, Saint-Aubin, France

⁷Department of Engineering "Enzo Ferrari", University of Modena and Reggio Emilia, 41125 Modena, Italy

Department of Engineering "Enzo Ferrari", University of Modena and Reggio Emilia, 41125 Modena, Italy Sam Nujoma Marine and Coastal Resources Research Centre, University of Namibia, Henties Bay, Namibia ⁹Climatology Research Group, North-West University, Potchefstroom, South Africa anow at: INRAE, Palaiseau, France

Correspondence: Paola Formenti (paola.formenti@lisa.ipsl.fr)

Received: 8 February 2025 – Discussion started: 8 April 2025 Revised: 16 July 2025 – Accepted: 17 July 2025 – Published: 19 November 2025

Abstract. This paper presents the results of 3 weeks of aerosol sampling at the Henties Bay coastal site in Namibia during the Aerosols, Radiation and Clouds in southern Africa (AEROCLO-sA) field campaign in August–September 2017. The campaign coincided with a transition period between two synoptic regimes and corresponded to a significant change in the aerosol composition measured at the site and in particular of that of mineral dust. During August, the dust was natural windblown from the southerly gravel plains, with a composition consistent with that previously observed in Namibia. In September, the dust was fugitive from anthropogenic mining, possibly with a minor contribution of smelting emissions in northern Namibia or as far as the Copper Belt in Zambia, one of the regional hotspots of pollution.

Chemical analysis of filter samples highlights the difference in elemental composition, in particular heavy metals, such as As, Cu, Cd, Pb, and Zn, but also silicon, in the anthropogenic dust. The metal solubility of the natural dust was higher, including that of iron (up to 5% compared to less than 1% for anthropogenic dust). Anthropogenic dust was associated with slight higher content of iron oxides and a larger proportion of coarse particles. Additionally, we found that the iron solubility, and, more in general, the metals' solubility, correlated to the high concentrations of fluoride ions which are attributed to marine emissions from the Namibian shelf. In a renewed manner, these results highlight the importance of ocean–atmosphere exchanges affecting both the atmospheric composition and the marine biogeochemistry in the Benguela region.

1 Introduction

Mineral dust is an abundant component of the global atmosphere (Kok et al., 2023). Dust particles in the atmosphere are released by the natural wind erosion of natural arid and semiarid areas of the globe. However, between 20 % and 30 % of global dust emissions are also contributed by anthropogenic activities such as labouring of bare soils for agriculture, pasture, or construction but also fugitive dust from mining and road traffic activities (Knippertz and Stuut, 2014; Chen et al., 2023). Mineral dust is a strong regulator of the Earth's climate and environment (Kok et al., 2023). In the atmosphere, it contributes to both the direct and indirect radiative effects on climate by scattering and absorbing solar and terrestrial radiation and forming cloud droplets in the liquid and ice phases (Kok et al., 2023). It also affects the atmospheric composition and oxidative capacity by acting as a source or a reactive sink of species from the gas phase (Usher et al., 2003). It also acts as an irritating agent for the upper respiratory system and a vector of bacteria and infections (Adebiyi et al., 2023). By deposition, mineral dust can provide nutrients and pollutants to the sea water, changing the ocean's primary production (Knippertz and Stuut, 2014).

These considerations apply to the west coast of southern Africa, and Namibia in particular, a hyper-arid climate where many dust sources co-exist (Vickery et al., 2013). Natural mineral dust is emitted from coastal riverine sources, salty pans such as the Etosha, and large gravel plains ubiquitous around the country (Vickery et al., 2013; Dansie et al., 2017a; von Holdt and Eckardt, 2018; Klopper et al., 2020; Shikwambana and Kganyago, 2022; Desboeufs et al., 2024). These sources are active throughout the year as emissions occur under various wind regimes (von Holdt and Eckardt, 2018). Natural mineral dust from Namibia is transported within the shallow boundary layer but being able to reach as far as Eastern Antarctica through long-range transport (Gili et al., 2022). Previous research in Namibia has shown that natural mineral dust from the coastal riverbeds and the gravel plains might contribute to oceanic productivity, particularly along the coast (Dansie et al., 2022). This research also pointed to iron as a highly soluble element in both the soil and windblown aerosol fraction and the control for the impact of dust on oceanic productivity (Dansie et al., 2017a, b, 2018; Desboeufs et al., 2024).

Furthermore, coastal pollution is an emerging issue of the present-day world (Strain et al., 2022). Increased human activities and coastal developments are quickly affecting the air quality but also the aquatic environment and biodiversity (Micella et al., 2024). Indeed, and despite its low population, Namibia also has intense and emerging economic activities such as mining (various heavy elements, including uranium; Mileusnić et al., 2014; Sracek, 2015; Liebenberg-Enslin et al., 2020) and marine traffic transporting merchandise along the coast of Africa and towards South America (Tournadre, 2014; Klopper et al., 2020). These activities re-

lease fugitive dust from the mine locations as well as from the numerous road constructions from and to the major national harbour, Walvis Bay (https://mwt.gov.na/projects, last access: 26 November 2024). In Namibia, the accumulation of heavy metals in the shore and coastal waters due to coastal mining (Onjefu et al., 2020) has been previously documented (Sylvanus et al., 2016; Omoregie et al., 2019; Nekhoroshkov et al., 2021). Furthermore, in the austral wintertime, Namibia is affected by anti-cyclonic circulation, resulting in the transport of light-absorbing particles, likely from forest fires and mining areas such as the Zambian Copper Belt (Formenti et al., 2018; Aurélien et al., 2022; Martinez-Alonso et al., 2023; Kříbek et al., 2023). The composition of these emissions is little characterized to date, though they have the potential to alter the oceanic productivity and microbial biogeochemistry (Adriano, 2001; Jordi et al., 2012; Mahowald et al., 2018; Yang et al., 2019).

In this paper, we present a case study analysis of the differences and similarities of the composition of natural and anthropogenic mineral dust sampled during the ground-based field campaign of the Aerosols, Radiation and Clouds in southern Africa (AEROCLO-sA) project (Formenti et al., 2019). The campaign was conducted in August–September 2017 in Henties Bay (22°6′ S, 14°30′ E; 20 m a.s.l.) along the Namibian coast.

Based on analysis of the chemical composition and meteorological fields, we demonstrate the origin of the anthropogenic dust and contrast its elemental composition, iron mineralogy and solubility, and the type of organic matter with respect to those of natural dust measured at the beginning of the campaign. Our analysis focusses on the iron mineralogy and solubility but includes, for the first time, the evaluation of the solubility of heavy metals transported with these emissions.

2 Experiment

The AEROCLO-sA field campaign took place from 21 August to 13 September 2017 at the Sam Nujoma Marine and Coastal Resources Research Centre (SANUMARC) of the University of Namibia at Henties Bay (Formenti et al., 2019). This sampling site, that has operated in the long term as described by Formenti et al. (2018) and Klopper et al. (2020), was augmented with the PortablE Gas and Aerosol Sampling UnitS (PEGASUS; https://pegasus.aeris-data.fr/, last access: 24 January 2025) mobile facility for the time of the campaign.

The PEGASUS facility consists of two marine containers (20 ft or 6 m long) customized and equipped for atmospheric research (Formenti et al., 2019). Air sampling is performed with two high-volume aerosol inlets delivering approximately $450 \, \mathrm{L\,min^{-1}}$ each. At wind speeds between 5 and $10 \, \mathrm{m\,s^{-1}}$, typical for coastal Namibia (see Fig. S1 in the Supplement), sampling is almost isokinetic for particles up

to $40\,\mu m$ in aerodynamic diameter (Rajot et al., 2008), which hereafter we named total suspended particulate (TSP). The total sampled flow rate is distributed to online analysers and to multiple- and single-stack sample collection units for off-line analysis of the bulk and size-resolved chemical and mineralogical composition, soluble fraction, and mixing state. The details of the online instrumentation relevant to this publication are listed in Table S1.

2.1 Sample collection

During the campaign, aerosol samples were collected during both the daytime (approximately 07:00–17:00 UTC) and the night-time (approximately 17:30–06:30 UTC). The sampling duration was marginally adapted in real time to the nature and the aerosol load of air masses using the readings of the local wind speed and direction and of the aerosol mass concentration, also measured online.

Four custom-made filter holders were used in parallel for collecting aerosols in the TSP fraction. These were loaded with (i) one Teflon filter (Zefluor[®], 2 µm pore size diameter, 47-mm filter diameter), (ii) two polycarbonate membranes (Nuclepore[®], 0.4 µm pore size diameter, 37 and 47 mm filter diameter, respectively), and (iii) a quartz filter (Pall, 2500QAT-UP Tissuquartz, 47 mm filter diameter). The average sampling flow rate varied between 20 and 30 L min⁻¹.

Two samples of the composition of particles smaller than 1 μ m in diameter (hereafter named PM₁ size fraction) were collected in parallel using two 4-stage Dekati[®] PM₁₀ Impactors, both operated at $10\,L\,\text{min}^{-1}$. For these two samplers we used 25 mm polycarbonate membranes on three impactor stages (> 10, 10–2.5 and 2.5–1 μ m), while the final filter stage, where the PM₁ fraction is collected, was a polycarbonate membrane (Nuclepore[®], 0.4 μ m pore size, 47-mm filter diameter) and a quartz filter (Pall, 2500QAT-UP Tissuquartz, 47 mm filter diameter), respectively.

Before the campaign, Teflon and quartz membranes were cleaned for sampling organic aerosols. Teflon membranes were rinsed with dichloromethane and baked at $100\,^{\circ}$ C for $10\,\text{min}$. Quartz membranes were baked at $550\,^{\circ}$ C for $12\,\text{h}$. Both were conditioned in pre-baked aluminium foils. The polycarbonate membranes were used for measuring the inorganic and water-soluble fraction composition. The 37 and 25 mm membranes were used as purchased, while the 47 mm ones were acid-washed according to the protocol described in Desboeufs et al. (2024). All material was sealed and opened only before collection. Immediately after exposure, all samples were sealed and stored at $-18\,^{\circ}$ C in the deep freezer available in the PEGASUS facility, from which they were transported back to the laboratory.

TSP filter samples were collected between 21 August and 12 September 2017, while PM₁ samples were collected from 26 August 2017 onwards. In total, 36 TSP and 31 PM₁ samples were collected per filter type during the field campaign (including blanks).

2.2 Sample analysis

2.2.1 Elements and water-soluble ions

The analysis of the elemental and water-soluble ion concentrations was performed at LISA according to the protocols previously detailed in Klopper et al. (2020) and Desboeufs et al. (2024). The elemental concentrations of 24 elements (Na, Mg, Al, Si, P, S, Cl, K, Ca, Ti, V, Cr, Mn, Fe, Co, Ni, Cu, Zn, As, Sr, Pb, Nd, Cd, Ba) were measured by wavelengthdispersive X-ray fluorescence (WD-XRF) using a PW-2404 spectrometer (Panalytical, Almelo, Netherlands). The instrument was calibrated with mono- and bi-elemental certified elemental standards (Micromatter Inc., Surrey, Canada). The concentrations of light-weight elements (Na to Ca) in the TSP fraction were corrected for X-ray self-attenuation as described in Formenti et al. (2010), assuming a mean diameter of 4.5 µm to represent the average coarse particle size. Elements heavier than Ca, as well as concentrations measured in the PM₁ fraction, were not corrected. The measured atmospheric concentrations are expressed in ng m⁻³, and the relative analytical uncertainty was evaluated as 10 % (see Klopper et al. (2020) for the full description).

The analysis of the water-soluble fraction was performed by extracting the filters with 20 mL of ultrapure water (MilliQ® 18.2 M Ω cm) for 30 min. The solution was divided into two sub-samples filtered to 0.2 µm of porosity (Nuclepore). One-half was analysed by ion chromatography (IC) using a Metrohm IC 850 device equipped with a column MetrosepA supp 7 (250/4.0 mm) for anions and with a Metrosep C4 (250/4.0 mm) for cations. The IC analysis provided the concentrations of the following water-soluble ions: F $^-$, formate, acetate, MSA $^-$ (methanesulfonic acid), Cl $^-$, NO $^-_3$, SO $^{2-}_4$, oxalate, Na $^+$, NH $^+_4$, K $^+$, Ca $^{2+}$, and Mg $^{2+}$. A calibration with certified standard multi-ions solutions of concentrations ranging from 5 to 5000 ppb was performed, and the uncertainty of the analysis was estimated to be 5 % (Klopper et al., 2020).

The second half of the solution was acidified to 1% with ultrapure nitric acid (HNO₃) and analysed by a combination of inductively coupled plasma-atomic emission spectroscopy (ICP AES) using Spectro ARCOS Ametek® ICP-AES and by high-resolution inductively coupled plasmamass spectrometry (HR-ICP-MS) using a Neptune Plus instrument by Thermo Scientific as described in Desboeufs et al. (2024). The calibration curve was performed using standard multi-element solutions ranging from 1 to 1000 ppt. The elemental fractional solubility (FS) of elements is calculated as the ratio between the dissolved and the total concentration.

Organic carbon (OC) and elemental carbon (EC) were measured using a thermo-optical carbon analyser (Sunset Laboratory Inc.) on a 1.5 cm² filter following the EUSSAR-II protocol (Cavalli et al., 2010). The Sunset analyser was calibrated using a sucrose solution (purity > 99.5 %) in the concentration range between 0.42 and $40\,\mu g\,cm^{-2}$. The limit of

quantification for total carbon and organic carbon is henceforth estimated to be equal to $0.42\,\mu g\,cm^{-2}$. An instrumental blank and a control point with a sucrose solution at $10\,\mu g\,cm^{-2}$ were done at the beginning of each day of analysis. OC and EC concentrations are automatically calculated with the software OCBC835 (Sunset Laboratory). The optical split point was manually verified to ensure their assignment.

All the concentration values presented in this paper were corrected for the average concentration measured for their corresponding analytical blanks, which was almost equal to the limit of detection.

2.2.2 Iron mineralogy

The quantification of iron oxides and the partitioning of iron species in the II and III oxidation state was performed by X-Ray Absorption (XAS) analysis at the Fe K-edge. Analysis was performed on the Teflon TSP filters only as the concentrations of the PM₁ filters were not high enough for this kind of analysis.

XAS analysis was conducted at the SAMBA (Spectroscopies Applied to Materials based on Absorption) line at the SOLEIL synchrotron facility in Saclay, France (Briois et al., 2011), according to the protocols and procedures previously presented in Formenti et al. (2014) and Caponi et al. (2017). A Si(220) double-crystal monochromator was used to produce a monochromatic X-ray beam, which was $4000 \times 1000 \, \mu \text{m}^2$ in size at the focal point. The energy of the X-ray beam was calibrated with an external Fe foil standard before the experiments. The energy range was scanned from $7050 \, \text{to} \, 7350 \, \text{eV}$ at a step resolution of $0.2 \, \text{eV}$.

Aerosol samples were mounted in an external setup. A portion of each aerosol filter sample was cut and mounted on a carton board holder with five available positions and analysed in fluorescence mode without prior preparation. The number of scans per sample was set between 50 and 200, depending on the iron concentration, to improve the signal-tonoise ratio. One scan acquisition lasted approximately 100 s for a total of 1.3 to 5.5 h of measurements for 50 to 200 scans.

The spectral analysis was conducted with the FASTOSH software package developed at SAMBA. As described in Wilke et al. (2001) and O'Day et al. (2004), the oxidation state and the bonding environment of Fe in dust samples give rise to different features in the XAS spectra. In the pre-edge region, the shape of the XAS spectra is determined by electronic transitions to empty bound states, which are strongly influenced by the oxidation state of the absorbing atom but also by the local geometry around the absorbing atom due to hybridization effects. Wilke et al. (2001) found that for Fe(II)-bearing minerals, the position of the centroid of the pre-edge is found at 7112.1 eV, whereas it is at 7113.5 eV for Fe(III)-bearing minerals. The position of the rising edge, which also depends on the oxidation state, is found at approximately 7120 eV. In the X-ray Absorption Near Edge

Structure (XANES) region, extending approximately 50 eV above the K-edge peak, features are determined by multiple-scattering resonances of the photo-electron ejected at low kinetic energies.

The speciation of Fe was obtained by the least-squares fit of the measured XANES spectra based on the linear combination of mineralogical references. Fits were conducted on the first derivative of the normalized spectral absorbance in the energy region between 7100 and 7180 eV, corresponding to -30 and +50 eV of the K-edge. Only the fits with a χ^2 closest to 1 were retained for further analysis.

The reference standards were chosen based on the expected iron mineralogy in the area (White et al., 2007; Heine and Völkel, 2010; Formenti et al., 2014; Sracek, 2015; Zhang et al., 2022). Standards for clays (illite and montmorrilonite) and iron oxides as goethite, magnetite, and hematite were taken from Formenti et al. (2014) and Baldo et al. (2020). The ferrihydrite standard was derived by the database of the Advanced Light Source, Lawrence Berkeley National Lab (Sirine Frakra, personal communication, 2008). Standards for metal-ligand complexes expected to form in fog droplets and deliquescent aerosol at high RH (Giorio et al., 2022) is provided in Table S2.

2.2.3 Organic analysis

The water-soluble fraction of organic aerosols (WSOC) was extracted, purified using hydrophobic resin (Bond Elut ppl), and analysed by high-resolution mass spectrometry (HRMS), namely by a hybrid LTQ-Orbitrap equipped with an electrospray source (ESI) operated in negative ion mode. All the samples were directly injected into the ESI source using a syringe pump. In each case spectra were recorded in triplicates in two mass diapasons to decrease the number of ions in the detector: $50-500 \ m/z$ and $150-700 \ m/z$. Raw spectra were treated following the laboratory procedure reported in Zherebker et al. (2024). Files were converted to *.mzML format using msconvert with a vendor-recommended peak-picking algorithm (https://proteowizard.sourceforge.io/, last access: 18 December 2024), which was suitable for a series of in-house written Python scripts, which included de-noising, calibration, formulae assignment, and blank subtraction. Only formulae presented in triplicates were retained. Diapasons were combined with removing lower-intensity duplicates. Formulae assignment was performed considering only singlecharged ions, ignoring anion radicals with the following atomic constraints: O/C ratio ≤ 2 , 0.3 < H/C ratio < 2.5; element counts $[1 < C \le 60, 2 < H \le 100, 0 < O \le 60, N \le 2,$ S < 1]. Each formula was attributed to the tentative chemical class (Table S4) based on the constrained aromaticity index (AI_{con}) calculated according to Zherebker et al. (2024). In addition, the double-bond equivalent (DBE) has been calculated, which represents the sum of sp² and sp bonds and cycles. Further details of the mass spectrometry results are provided in Text S1.

2.3 Ancillary products

2.3.1 Air mass back trajectories

Three-dimensional air mass back-trajectory ensembles are calculated using the NOAA HYbrid Single-Particle Lagrangian Integrated Trajectory Model (HYSPLIT; Stein et al., 2015). The Weather Research and Forecasting model (WRF, version 3.71; Skamarock et al., 2008) forced by Operational Global Analysis data (NCEP: National Centers for Environmental Prediction; GDAS: Global Data Assimilation System, https://rda.ucar.edu/datasets/d083002, last access: 10 January 2025) was used to simulated hourly meteorological data at 50 and 9 km horizontal resolution.

2.3.2 Atmospheric circulation

The atmospheric circulation and composition at the regional scale from 21 August to 13 September 2017 were further investigated using the Copernicus Atmospheric Monitoring Service (CAMS) reanalysis (Inness et al., 2019), available every 3 h from 00:00 to 21:00 UTC. The spatial resolution is approximately 80 km and 60 pressure levels (37 of which are below 20 km and 20 below 5 km). The atmospheric composition is described by analysing the total aerosol optical depth (AOD) at 550 nm and the mass mixing ratio of dust and sulfate aerosols. The atmospheric circulation is described by analysing the near-surface (10 m) wind, to highlight emission processes and local transport, and the geopotential height at 700 hPa, to highlight the large-scale circulation and longrange transport. Atmospheric composition and circulation data are averaged at the daily timescale.

2.3.3 Positive matrix factorization analysis

Positive matrix factorization (PMF) (Paatero, 1997; Paatero and Tapper, 1994) was applied to chemical composition data (OC, EC, inorganic ions, and total metals) of TSP and PM₁ samples using the software EPA PMF 5.0. Different factor solutions were investigated in the range of 3 to 8 factors, starting from 10 different seeds. The 4-factor solution and the 3-factor solution were selected for TSP and PM₁, respectively, based on the inflexion point of Q/Qexp and chemical interpretation of the resulting factor profiles (loadings). The selected solutions were run again from 100 different seeds, and the solutions with the lowest Q were selected. Rotational ambiguity was investigated by changing the Fpeak parameter from 0 to \pm 0.5 and \pm 1. The solutions with Fpeak = 0 were selected, and bootstrap analysis was performed using a number of bootstraps of 100 and a minimum r value of 0.6.

3 Results

3.1 Air mass origin and local meteorology

Chazette et al. (2019) and Gaetani et al. (2021) showed that mid-tropospheric air masses during the field campaign were characterized by three distinct periods. In the first period (P1; 22-28 August 2017), air masses were southerly and characterized by low aerosol content and large particles. From 23 to 25 August, the circulation in the middle troposphere was characterized by the reinforcement of the South Atlantic anticyclone, leading to prevailing south-westerly winds above Namibia (Fig. S2). From 26 to 28 August, the transit of a disturbance in the Southern Ocean was accompanied by the installation of the continental high and prevailing northwesterly winds above Namibia (Fig. S2). In the second period (P2; 29 August—1 September 2017), the circulation was characterized by the weakening of the South Atlantic anticyclone and the reinforcement of the continental high (Fig. S2), associated with a northerly/easterly flow and transport of recirculation of a higher load of aerosols associated with biomass burning. The circulation pattern remained the same in the third period (P3; 3–12 September 2017), but the aerosol content further increased. After the transit of a cut-off low in the upper troposphere on 2-4 September (Flamant et al., 2022), the large-scale circulation was dominated by the further reinforcement of the continental high and, on the 8–9 September, by the installation of a trough over the South Atlantic, leading to favourable conditions for the recirculation of continental aerosol towards Namibia.

The same synoptic circulation was observed at the surface level. Air mass back trajectories (Fig. S3) show that the air flow at the surface level was southerly during P1 and P2 but shifted to north-easterly (continental) after 2 September (P3), when the frequency of the anti-cyclonic circulation towards Henties Bay increased. Continental air masses generally took more than 2 d to reach the site. In the last 2 d of transport, they moved along the coast or recirculated around Henties Bay, alternating the S-SW and NW-NNW directions. In a few cases, and in particular on 11 September, the transport of continental air masses was more direct and within 2 d from Henties Bay. The record of local winds measured during the campaign (Fig. S1 in the Supplement) testifies of the frequent recirculation. Strong winds (average 5 m s⁻¹, and up to $10\,\mathrm{m\,s^{-1}})$ came, alternatively, from the S-SW direction (20-22 August, 29-31 August, 6-9 September, 11 September, grey boxes in Fig. S1) and the NW-NNW direction (23-28 August, 1-5 September, 10 September, 12-13 September). Occasionally, a gentle land breeze (easterly winds below 2 m s⁻¹) was observed before sunrise or after sunset. In general terms, as discussed in Giorio et al. (2022), the local meteorological conditions at Henties Bay during the campaign were characterized by remarkable stability in terms of temperature (around 12 °C) and humidity (RH ~ 95 %), while a persistent stratocumulus cloud deck kept solar irradiance below 600 W m^{-2} .

3.2 Aerosol composition and origin

The summary statistics of the aerosol composition is reported in Table S3. The TSP chemical composition was dominated by the sea-salt tracers, Na $^+$ and Cl $^-$ (average \pm standard deviation concentrations of 22 ± 11 and $39\pm21\,\mu g\,m^{-3}$, respectively), as well as SO_4^{2-} (9.1 $\pm4.3\,\mu g\,m^{-3}$), Mg $^{2+}$ (3.9 $\pm2.0\,\mu g\,m^{-3}$), K $^+$ (1.2 $\pm0.6\,\mu g\,m^{-3}$), and Ca $^{2+}$ (1.7 $\pm0.8\,\mu g\,m^{-3}$). In terms of metals and metalloids, A1 (0.6 $\pm0.4\,\mu g\,m^{-3}$), Fe (0.6 $\pm0.4\,\mu g\,m^{-3}$), and Si (2.5 $\pm1.3\,\mu g\,m^{-3}$) had the highest concentrations. The mean OC and EC concentrations were 3.2 ±1.5 and 0.2 $\pm0.2\,\mu g\,m^{-3}$, respectively. In the PM $_1$ fraction, due to the low flow rate used for sampling (10 L min $^{-1}$), only the major elements and ions were detected, in lower concentrations than in the TSP.

These observations are reflected in the results of the PMF analysis shown in Fig. 1.

The PMF analysis returned four factors in the TSP fraction and three in the PM₁ fraction, whose chemical fingerprints shown in Fig. S4. For the TSP aerosols, the "sea spray", represented by high loadings of Na⁺, Cl⁻, Mg²⁺, SO₄²⁻, and OC (Fig. S4), is the dominant factor with a concentration of up to $135 \,\mu\mathrm{g}\,\mathrm{m}^{-3}$, contributing on average to $46 \,\%$ of the aerosol mass (Fig. 1). It peaks during the initial part of the campaign and when winds blew from the ocean. The second most dominant factor is "secondary aerosol", contributing on average to 25.2% of the aerosol mass and characterized by high loadings of NO₃, SO₄²⁻, oxalate, and NH₄⁺, as well as OC. It is characterized also by high loadings of Na⁺ and Cl⁻ but an anti-correlation with the sea spray factor (r = -0.44), so rather than being a purely secondary aerosol factor it can be considered an aged sea spray. Its contribution increases toward the second part of the campaign, and it is generally higher during the day, due to enhanced photooxidation. These two factors were also extracted for PM₁. In the case of PM₁, the anti-correlation of these two factors is stronger than in TSP (r = -0.72 in PM₁, r = -0.44 in TSP).

Two factors characterized by a high loading of metals are identified: a "mineral dust" factor, characterized by high loadings of Al, Fe, and Si, as well as Ti, Mn, Na⁺, Ca²⁺, and SO₄², accounting for 5.8 % of the TSP aerosol mass and for 15 % of the PM₁ aerosol mass. In the TSP fraction only, a "Si-rich" factor accounting for 23.3 % of the aerosol mass is also identified. This factor, characterized by the presence of a high loading of Si, As, and Pb, strongly correlated to each other (r = 0.97), as well as moderate loadings of Co, Cu, Ni, Nd, Sr, and Zn, but not associated with Al and Fe (Fig. S4), will be discussed in the following sections.

3.2.1 Marine aerosols

Figure 2 presents the time series of the elemental concentrations of Na^+ and Cl^- and their ratios (Cl^-/Na^+) in the TSP and PM_1 fractions.

The concentrations of Na $^+$ and Cl $^-$, strongly correlated as expected, showed a relatively constant background of approximately $10\,\mu g\,m^{-3}$ (TSP) and $0.3\,\mu g\,m^{-3}$ (PM $_1$) and intense peaks of concentrations. In the TSP fraction, the Cl $^-$ concentration was up to $80\,\mu g\,m^{-3}$. The Cl $^-$ /Na $^+$ ratio was of the order of 1.5 in the P1 and P2 periods and of the order of 1.8 afterwards. In the PM $_1$ fraction, the Cl $^-$ concentration reached 2.5 $\mu g\,m^{-3}$. The Cl $^-$ /Na $^+$ ratio, little documented during P1, was around 0.7, while it increased between 1 and 1.8 during P2 and P3. Values of the order of 1.5–1.8 are consistent with the composition of local seawater (Giorio et al., 2025) and average sea spray (Seinfeld and Pandis, 2006), as well as the previous results by Klopper et al. (2020).

In both the TSP and PM_1 fractions, the mass concentration of organic carbon (OC) through the campaign was strongly associated with Na^+ as well as Cl^- (not shown). In the TSP fraction, where sufficient concentration allowed for robust measurements, the OC/Na^+ ratio was variable and ranged between 0.07 and 0.3, consistent with values reported by Frossard et al. (2014) for marine aerosol types. The molecular analysis of the organic composition provides insights into the sources affecting the OC/Na^+ ratio during the campaign (Fig. 3).

The differences in the molecular composition of samples from the P1-P3 periods are depicted in the van Krevelen diagrams (Fig. 3b-d), which highlight the unique molecular composition of each period. P1 was dominated by saturated and low oxidized (O/C < 0.3) CHO and CHON compounds, which occupy about 60% of the total molecular space (Fig. 3). This may indicate the high contribution of biogenic fatty acids and protein-derived compounds (Bikkina et al., 2019). Their cumulative contribution in P2 decreased to about 40 %, while a significant increase in the contribution of oxidized saturated compounds (O/C > 0.3) as well as highly unsaturated (AI_{con} >0.5) compounds was observed. Moreover, reduced (low O/C) saturated compounds appear to be unique for the P1 period (Fig. 3b). This supports the biogenic source brought by south-westerly winds. Further, the contribution of continental dust with a clear anthropogenic contribution is reflected as unique highly unsaturated compounds in the P2 period as well as an increase in S-containing compounds (Fig. 3c). P3 was depleted with highly unsaturated compounds, with a relative dominance of saturated Ncontaining compounds. The aerosol sources are similar between the P2 and P3 periods, which resulted in an insignificant amount of unique molecular assignment in the latter (Fig. 3d). In addition, the double-bond equivalent vs molecular mass diagram in the Supplement indicates an increase in the contribution of biomass-burning aerosols and possibly sulfate-enriched dust from smelting in the P2-P3 peri-

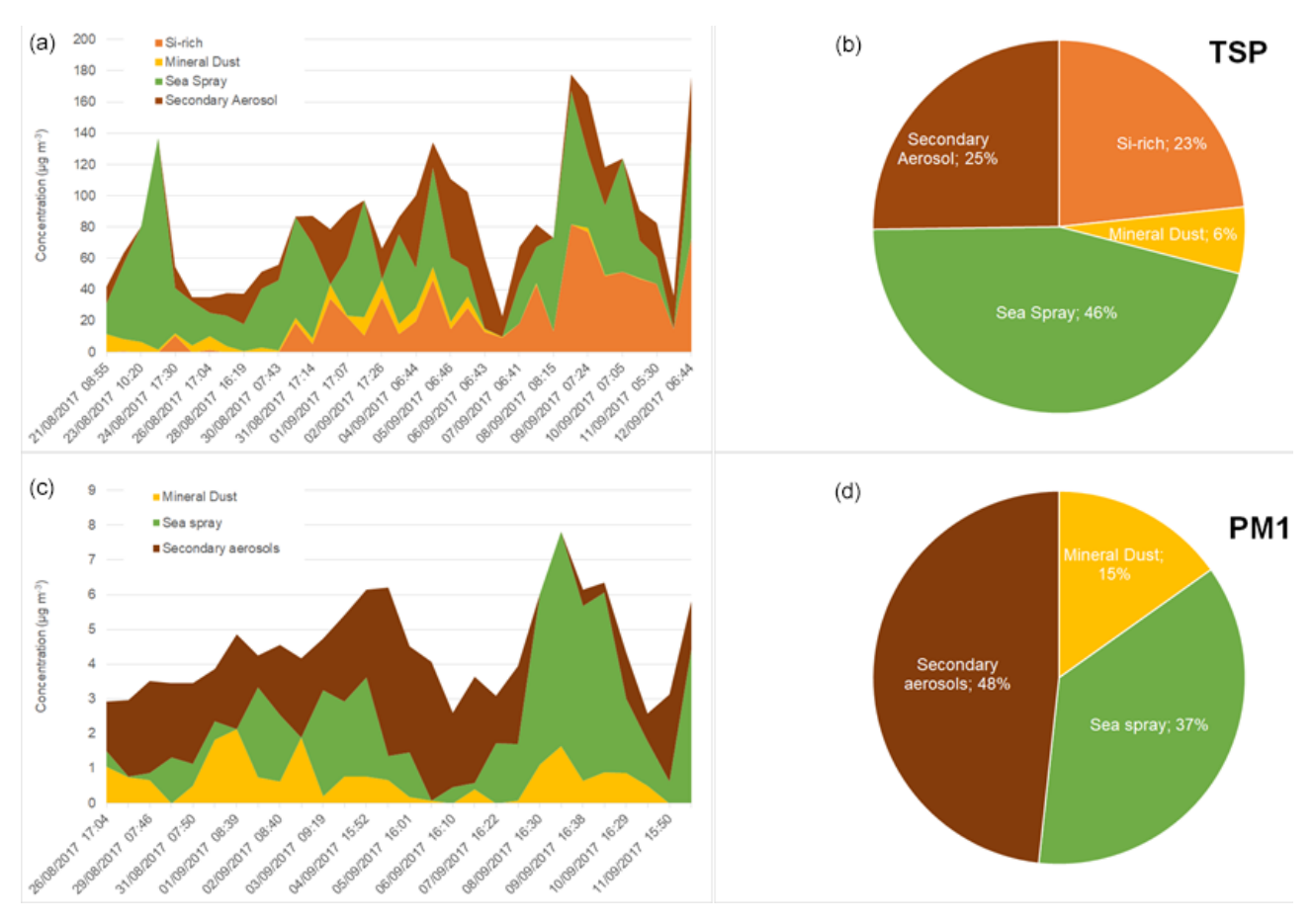


Figure 1. Time series of contributed concentrations ($\mu g \, m^{-3}$, a, c) and pie chart of average contributions of the factors obtained from the PMF analysis applied to TSP (a, b) and PM₁ (c, d) chemical compositions. Dates are reported as "DD/MM/YYYY hh:mm".

ods compared to the P1 period, which is in line with the air mass origin. Further details of the organic composition are reported in the Supplement.

3.2.2 Fluoride and MSA concentrations

The P1 and P2 periods were also characterized by extremely high concentrations of fluoride (up to $10\,\mu g\,m^{-3}$) as shown in Fig. 4, in line with what reported by Klopper et al. (2020) for the PM₁₀ aerosols measured during 2016 and 2017 at the site. In September (P3a and P3b), the concentration of F⁻ dropped to zero, as a consequence of the change in the origin of the air masses transported to the site.

Fluoride is a naturally occurring ion in marine environments as well as in mineral dust (Fuge, 2019). In Namibia, the release of dissolved fluoride to the atmosphere is due to the evaporation of fluoride-rich groundwater (Sracek et al., 2015) or the erosion of mineral deposits of calcium fluoride (CaF₂, Onipe et al., 2020). Fluoride is present in significant amounts (> 1 wt % F) in francolite, a carbonate fluorapatite mineral (typical formula Ca_{4.7}Na_{0.2}Mg_{0.1}(PO₄)_{2.6}(CO₃)_{0.4}F_{1.28}), which can be found

in phosphorite deposits on the Namibian shelf, notably in the area between 23 and 25.5° S south of Henties Bay (Compton and Bergh, 2016; Mänd et al., 2018). This could be the origin of the excessive fluoride concentrations observed during the P1 period of the campaign. Atlas and Pytkowicz (1977) and Hossein et al. (2024) describe the mechanism by which F could be released into seawater by dissolution. Upon dissolution, the release of F⁻ into the atmosphere can be attributed to the reaction with hydrogen in water to form hydrogen fluoride gas (or a solution of hydrofluoric acid; Anbar and Neta, 1967). The high content of fluoride in the Namibian soil is also documented and attributed to weathering and dissolution of fluoride-containing minerals (Hossein et al., 2024). Not only did the origin of air masses detected at Henties Bay coincide with the locations of the marine deposits, but during P1 the fluoride content also correlated with major marine tracers (Na, Cl, S; correlation coefficients $R^2 = 0.87$, 0.85 and 0.75, respectively). Fluoride correlated with calcium, both its sea-salt and non-sea-salt fractions (nss-Ca²⁺/F⁻ ratio ranging from 0.1 to 0.3, as in Klopper et al. (2020), correlation coefficients $R^2 = 0.67$ with nss-Ca²⁺ and 0.79 with Ca²⁺). Finally, fluoride also correlated with P, K, and Sr (cor-

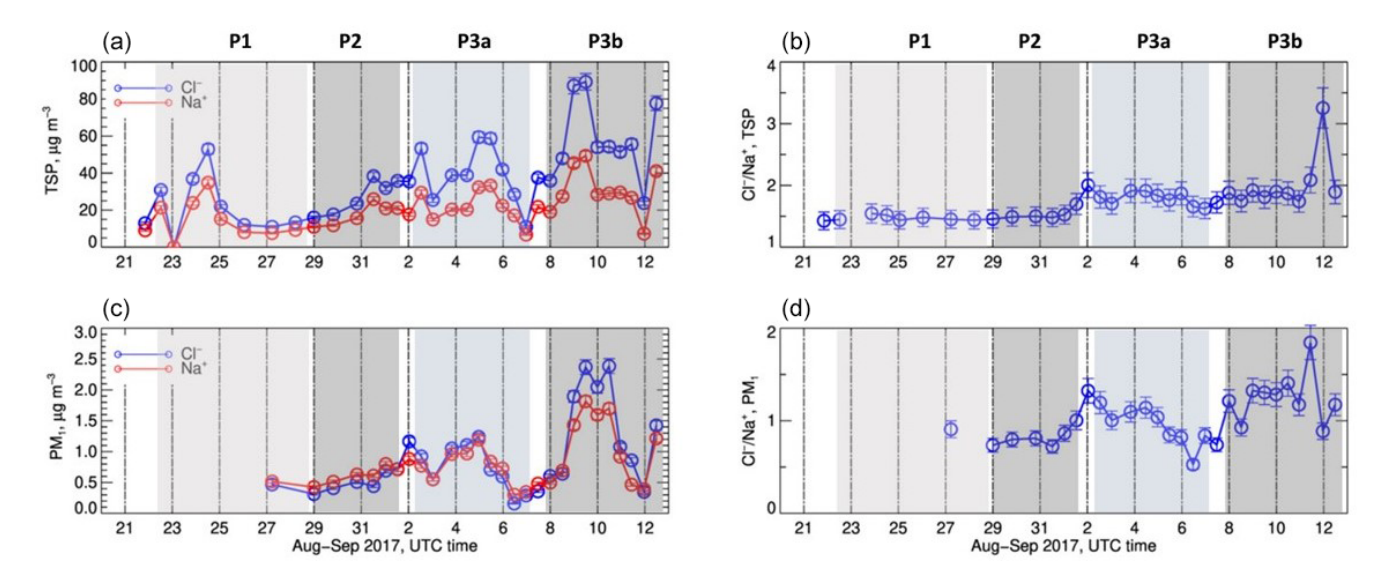


Figure 2. (a, c) Time series of the elemental concentrations of Cl^- and Na^+ in the TSP and PM_1 fractions. (b, d) Time series of elemental ratio of Cl^-/Na^+ in the TSP and PM_1 fractions. The grey panels represent the different meteorological periods. Error bars on concentrations represent the analytical errors. Error bars on ratios represent the sum of percent analytical errors on measured concentrations.

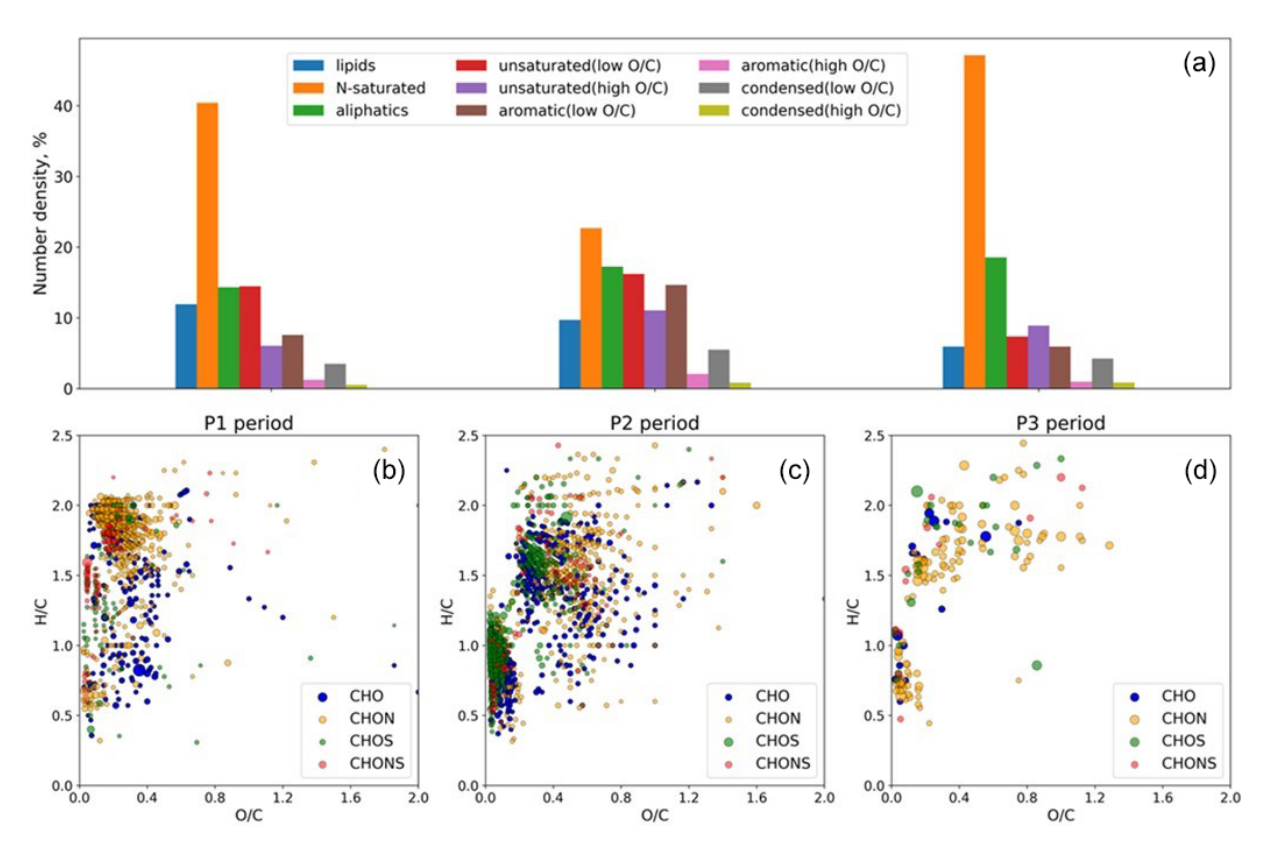


Figure 3. Population density of all molecular compositions based on AIcon classes (a) and van Krevelen diagrams for only unique molecular assignments in samples under study in the three periods (b-d), where unique formulae were only determined in a sample from the designated period. The size of the points reflects relative intensities in the mass spectra (not used in the analysis).

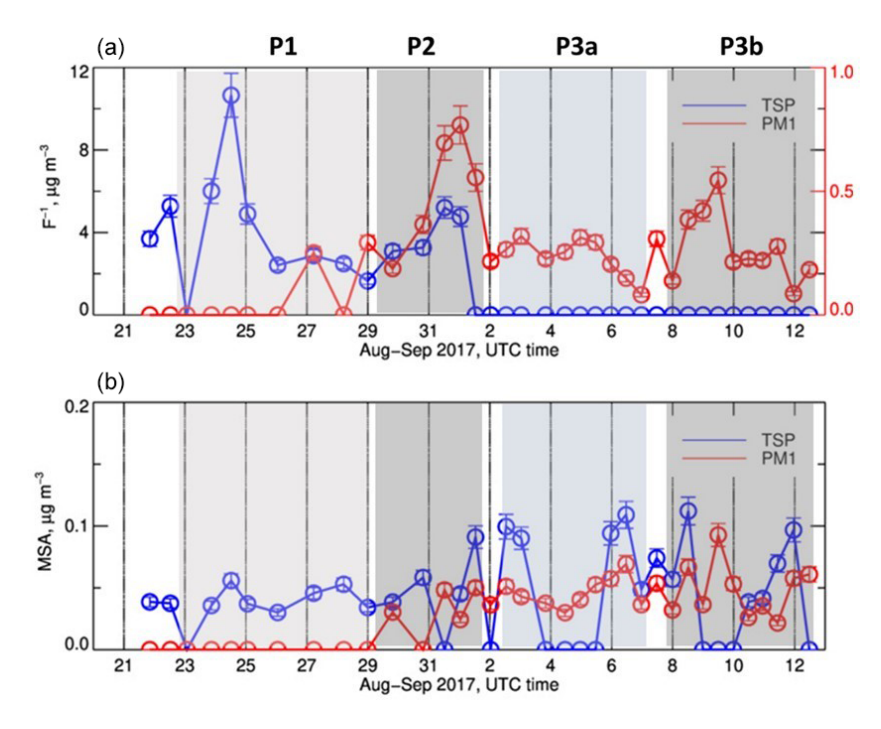


Figure 4. Time series of the elemental concentrations of F^- and MSA in the TSP (a) and PM₁ (b) fractions during the field campaign. Missing data correspond to periods when the measured concentrations were below the detection limits. Error bars on concentrations represent the analytical errors. Error bars on ratios represent the sum of percent analytical errors on measured concentrations.

relation coefficients $R^2 = 0.68$, 0.91, and 0.21, respectively); the latter can replace Ca in the francolite mineral structure (Compton and Bergh, 2016; Rakovan and Hughes, 2000). Note that, despite its high concentrations, fluoride was not included in the source apportionment because it was not measured during the whole field campaign.

The concentrations of methanesulfonic acid (MSA), a tracer of marine biogenic productivity, averaged at $61\pm26\,\mathrm{ng}\,\mathrm{m}^{-3}$ in the TSP fraction and $46\pm26\,\mathrm{ng}\,\mathrm{m}^{-3}$ in the PM $_1$ fraction. These values are consistent with the yearly average in the PM $_{10}$ reported by Klopper et al. (2020). While concentrations of F $^-$ and MSA appear unrelated in the TSP fraction, they remain above the detection limit in the PM $_1$ fraction, where they were measured starting from the P2 period only. While the F $^-$ concentrations showed a certain degree of variability, the MSA remained constant with time.

3.2.3 Mineral dust composition

Figure 5 presents the time series of the elemental concentrations of Al, Si, and Fe, major tracers of mineral dust, as well as of their ratios (Si/Al, Fe/Al, and Fe/Si) in the TSP and PM_1 fractions.

The elemental concentrations of Si and Al were up to 6 and $1 \mu g \, m^{-3}$ in the TSP fraction and up to 410 and 90 ng m⁻³ in the PM₁ fraction, respectively. In the P1 and P2 periods, and with the exception of a peak value on 24 August, the Si/Al ratio was of the order of 3.8, consistent with the findings of

Klopper et al. (2020) for natural mineral dust emitted from the Namibian gravel plains. After this date, that is during P3, the Si/Al ratio increased to values between 6 and 10 (TSP) and between 8 and 80 (PM $_1$), indicating a very strong enrichment with respect to the composition of the regional mineral dust.

In the TSP fraction, and regardless of the period, the Fe/Al ratio was in the range of 0.8–1.2, as previously found for the natural gravel plain dust in the area (Eltayeb et al., 1993; Klopper et al., 2020). Likewise, during P1 and P2 the Fe/Si ratio was consistent with those previous observations for mineral dust, and so was the Fe/Ca ratio (not shown), found in the range 0.2-0.8. However, during P3, the Fe/Si decreased from approximately 0.25 to 0.1, while the Fe/Ca ratio increased to between 0.09 and 0.15 (not shown). In the PM₁ fraction, both the Fe/Al and the Fe/Si ratios were more variable with time (only the September period is documented). The Fe/Al ratio was of the order of 1 as in the TSP fraction, except on the last day of the campaign when the ratio reached 18. The Fe/Si was higher between 29 August and 6 September (e.g. the P2 period), ranging from 0.2 to 0.4, and decreased to 0.1-0.2 in the last days of the campaign. That corresponded to the variability of several major elements and metals (K, Mg, Co, Cu, Nd, Ni, Sr, and Cd but Zn, As, and Pb in particular), whose ratios with Al were significantly higher during the last days of the campaign (7–12 September, Fig. S5). As for OC/Na⁺, the aerosol mineral composition of TSP during the P3 period could be split into

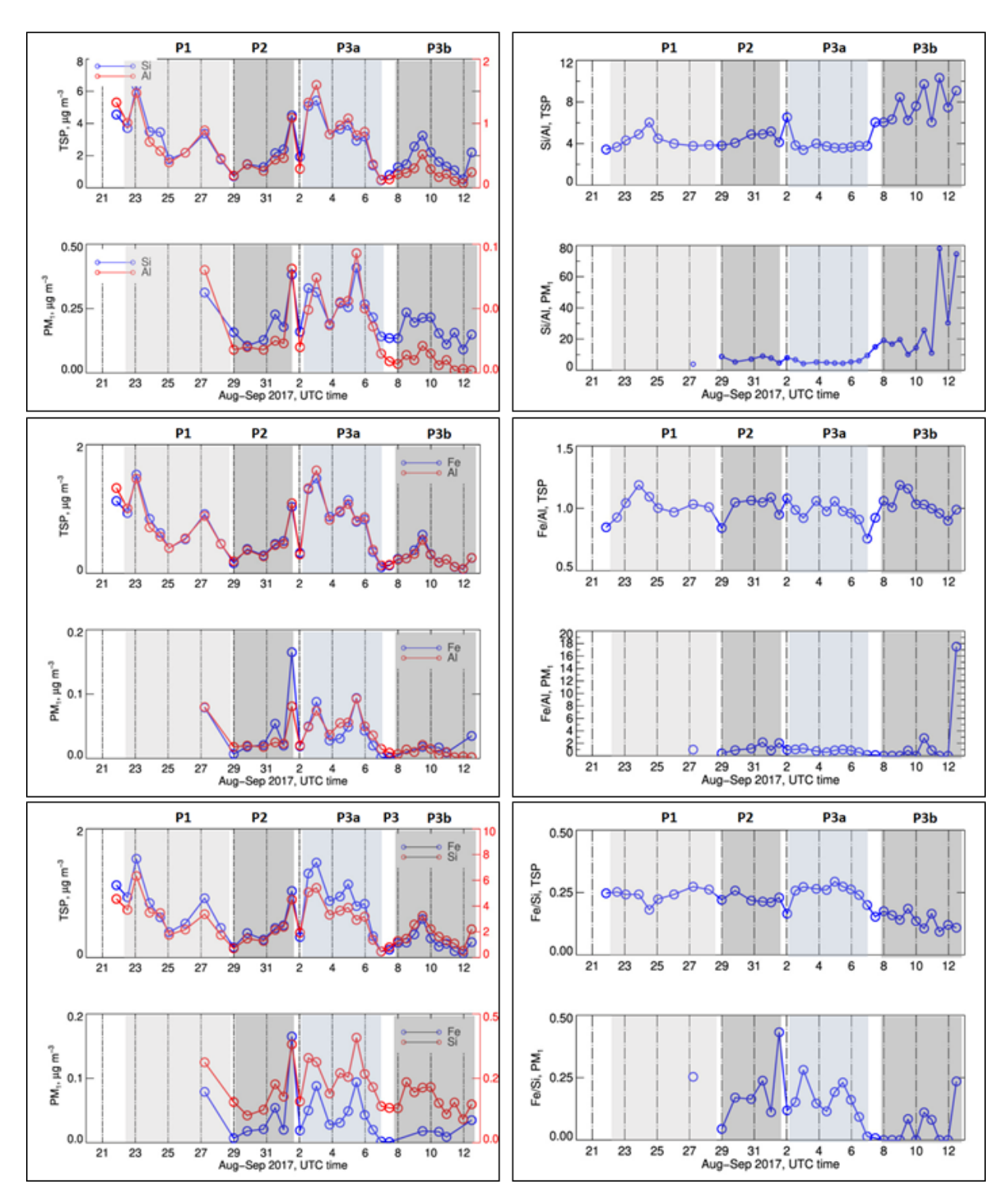


Figure 5. Left panel, from top to bottom: time series of the elemental concentrations Al, SI, and Fe in the TSP and PM_1 fractions. Right panel from top to bottom: time series of elemental ratio of Si/Al, Fe/Al and Fe/Si in TSP and PM_1 fractions. Missing data correspond to periods when the measured concentrations were below the detection limit. Error bars on concentrations represent the analytical errors. Error bars on ratios represent the sum of percent analytical errors on measured concentrations.

two sub-periods before and after 6 September, with an enrichment in metals and OC at the end of the campaign.

These observations are reflected by the PMF analysis, described in Text S2 in the Supplement. Note that, despite its high concentrations, fluoride was not included in the source apportionment because it was not measured during the whole field campaign. In the TSP fraction, the analysis separates two factors characterized by a high loading of metals. The first one is a "mineral dust" factor characterized by Al, Fe, and Si, as well as Ti, Mn, Na⁺, Ca²⁺, and SO₄²⁻. Its contribution, significant only during the first part of the campaign, accounted, on average, for 5.8 % of total TSP mass. The second factor, called "Si-rich", is characterized by the presence of a high loading of Si, As, and Pb, which are strongly correlated to each other (r = 0.97), and moderate loadings of Co, Cu, Ni, Nd, Sr, Zn, and EC, which are not correlated to Al or Fe, contrarily to "mineral dust". The "Si-rich" factor, significant mostly during the P3 period, notably after the 6 September, accounted for 23.3 % of TSP mass but was not found in the PM₁ fraction where the concentrations of the majority of its tracers were very close to the detection limit. This is in agreement with the fact that the fraction of coarse particles with respect to the total number increased on the last days of the campaign (Fig. S6).

The chemical fingerprinting of the "Si-rich" factor is similar to that reported from windblown dust from mines in the Otavi Mountainland in Namibia (Mileusnić et al., 2014; Sracek, 2015) as in the Zambian Copper Belt (Meter et al., 1999; Ettler et al., 2011, 2014; Mwaanga et al., 2019), a large and important mining area in the northern part of Zambia (Aurélien et al., 2022; Martínez-Alonso et al., 2023; Kříbek et al., 2023). Sracek (2015) found various associations of Fe with Cu, Co, Pb, V, As, Pb, and Zn for mines in Zambia and Namibia, characterized by different climates and ages of the core. At a receptor site on the Zambian Copperbelt in Zimbabwe, the analysis by Nyanganyura et al. (2007) identified the mixing of mineral dust and metal smelting emissions by distinguishing the long-range transport of aerosols containing Fe, Al, and Si but also Co from a non-ferrous smelter component contributing to the fine aerosol fraction only and characterized by S, Zn, As, and Pb. Ettler et al. (2014) indicated that iron is enriched with respect to both Al and Si in dust liberated from Cu-Co metal smelters in the Zambian Copperbelt. However, Meter et al. (1999) showed that enrichment is variable on an event basis depending on the pyro-metallurgical processing of ores and their composition.

We henceforth conclude that during P1 and P2 the aerosol composition was dominated by natural Namibian mineral dust sources with a composition very similar to the average dust composition measured at the same site in 2016–2017 (Klopper et al., 2020) and reaching the site within the southerly air flow. Conversely, during the last part of P3, the dust reaching Henties Bay was fugitive material from anthropogenic activities. The air masses during the second part of P3 could originate as far as from the Zambian Copper belt.

These conclusions are further corroborated by the CAMS reanalysis shown in Fig. S7. During P1 and P2 the dust mass mixing ratio reached up to $120 \,\mu g \, m^{-3}$ ($100 \,\mu g \, kg^{-1}$ on the CAMS map) at the surface in correspondence with the coastal sources in Namibia as a response to the prevailing south-easterly winds (Figure S3) dominating the near-surface circulation from 23 August to 3 September. Continental dust sources were activated on 22 August and 1 September, in association with south-westerly near-surface winds, and on 28-29 August and 4-5 September, in association with near-surface convergence of south-westerly and northeasterly winds. From 6 September onwards, no remarkable dust activity was observed, while the circulation had changed (Fig. S7). The CAMS reanalysis also showed that the sulfate mixing ratios at the surface reached $6 \mu g m^{-3}$ ($5 \mu g k g^{-1}$ on the CAMS map) in the Zambian Copper Belt and in the urban area of Pretoria and Johannesburg (Fig. S7), also a known pollution hotspot (Martínez-Alonso et al., 2023). Sulfate aerosols remained close to their source regions until the end P2. With the installation of the continental high on the 3 September, sulfate aerosols were recirculated southwestwards towards Henties Bay during P3, in particular during 10-12 September.

3.3 Iron mineralogy

The first derivative of the XANES normalized spectra for four samples collected during the different periods of AEROCLO-sA is shown in Fig. 6. The remaining spectra, including those of the standard minerals and compounds used for the deconvolution, are reported in Fig. S8.

Because of the small quantities of particle mass collected on the filters, the XANES spectra are rather noisy. The main features can nevertheless be explored after smoothing. They all are rather similar. In the region between 7122 and 7128 eV, two to three peaks are present with different intensities depending on the sample. The peak at 7128 eV is minor on sample T03 (P1 period), for which the peaks at 7122 and 7126 eV dominate. The peak at 7122 eV is not present afterwards. For samples T18 and T22 in the P2 period and the beginning of the P3 period, only the peaks at 7126 and 7128 eV are present, the intensity of the latter being higher than the one of the former, while those peaks have equal intensity on sample T032 in the P3 period. For mineral dust from northern Africa, Formenti et al. (2014) showed that the relative proportions of these peaks can be related to the type of clays but also to the presence of iron oxides in the form of hematite (Fe₂O₃) or goethite (FeOOH). Peaks between 7132 and 7136 eV are distinctive of clays and iron oxides in the form of hematite but are not present for goethite. In our samples, a minor shoulder in this spectral region is observed only for a few samples (T24, T25, and T31) collected in September. On the other hand, the pre-edge region between 7110 and 7116 eV is sensitive to the iron oxidation state. The majority of our samples seem to peak around 7113-7114 eV, indicat-

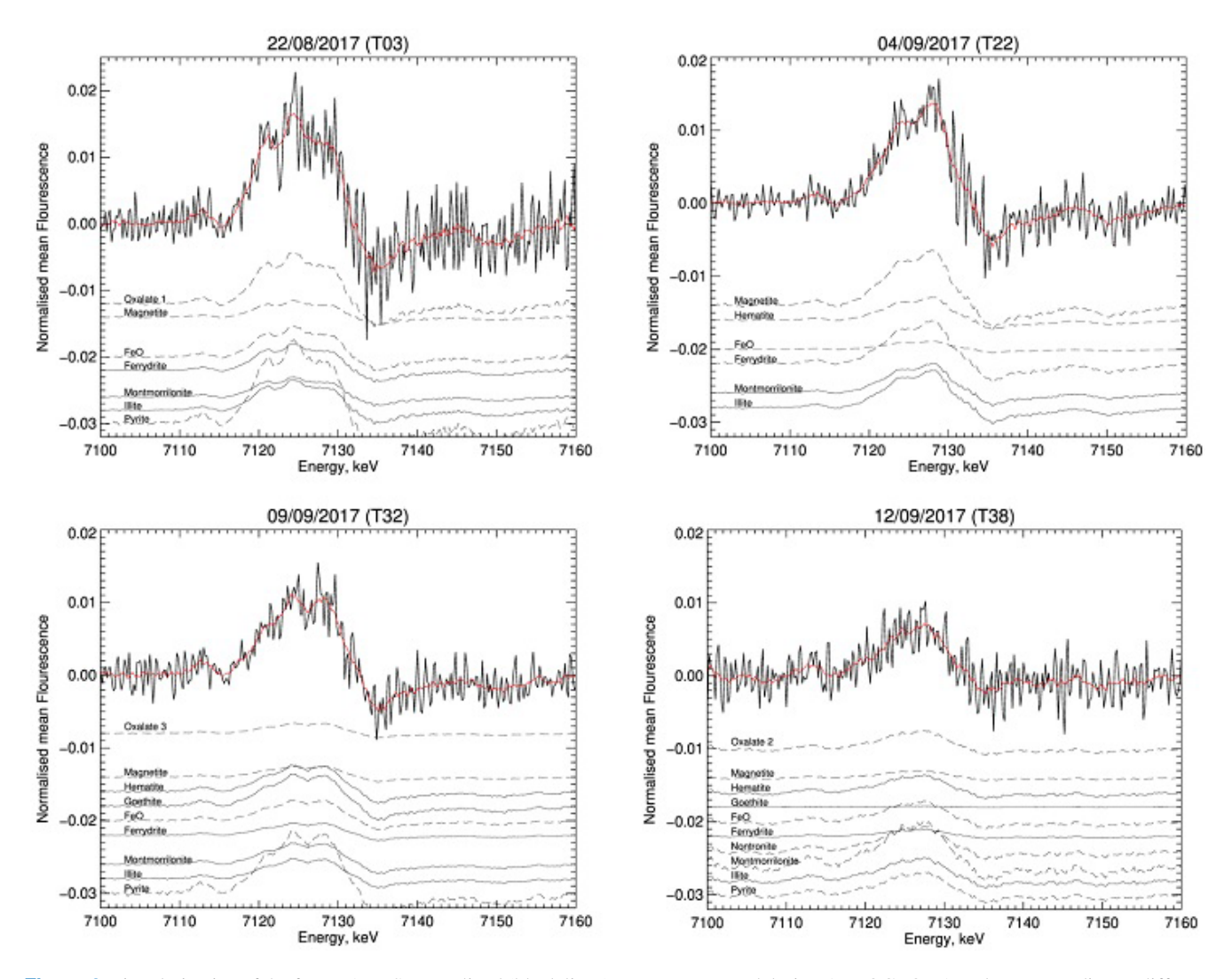


Figure 6. First derivative of the four XANES normalized (black lines) spectra measured during AEROCLO-sA and corresponding to different periods and mineralogy. The red lines correspond to the fitted spectra. The contribution of the individual standards to the total measured signal is also reported. The dotted lines represent the contributions smaller than 10%, which have been multiplied by a factor of 10 to ease their visualization.

ing that iron is predominantly in the Fe(III) oxidation state. Only for a few samples (T10, T25, T26, T30, and T37) is the pre-edge peak closer to 7112 eV, indicating that Fe(II) could be the predominant oxidation state.

Several attempts of least-squares reduction were done with a variable number of references to reflect the many mineralogical forms in which iron can be found and verify the stability of the solution. While the relative proportions might have changed by a few percent, the overall repartition was found to be consistent and independent of the selected references.

The average least-squares apportionment of the total TSP elemental iron is presented in Table 1 in terms of the mean fractions par sampling period and mineralogical classes.

The largest contribution to the total iron is by clays, between 42 % and 58 %, with illite and montmorillonite con-

tributing in equal proportions. While a clear temporal trend cannot be defined, the contribution of clays is lowest during the latest sampling period (6-12 September 2017). The second largest contribution is by iron oxides, accounting for between 38 % and 45 % of the total iron throughout the sampling period. The contribution of FeO, iron oxide in Fe(II) form, is low and extremely variable from sample to sample and not necessarily retrieved for samples in which a shift towards the Fe(II) seems evident in the pre-edge region (T10, T25, T26, T30, and T37). The P3 period is also characterized by the lowest contribution of Fe(III) oxide (64 % vs 72 %–75 %). Ferrihydrite $(14 \pm 7\%)$ of total iron and goethite (8 \pm 6 % of total iron) showed their highest contributions during P2 (21 % and 12 % respectively), while hematite (8 ± 6 of total iron) was highest in September (P3). Sracek (2015) found that the formation of secondary hematite is 7 ± 5

 17 ± 7

21-31 Aug 2017 1-2 Sep 2017 2-7 Sep 2017 8-12 Sep 2017 T01-T14 T15-T18 T20-T27 T28-T38 Clays 49 ± 13 58 ± 12 53 ± 11 42 ± 10 Goethite 10 ± 4 9 ± 2 6 ± 5 6 ± 3 Hematite 7 ± 5 8 ± 7 15 ± 11 9 ± 7 14 ± 6 Magnetite 10 ± 5 9 ± 8 15 ± 11 Oxalate 4 ± 4 3 ± 4 3 ± 4 5 ± 7

 3 ± 4

 14 ± 12

Table 1. Apportionment of total iron (percent mean and standard deviation) by the least-squares deconvolution of the XANES spectra obtained on the filter samples indicated in the first row. Results are grouped by period and by mineral class.

favoured by tropical climate conditions in mines in Zambia compared to Namibia. In contrast to northern African dust, the least-squares reduction shows that the presence of magnetite is significant in the dust collected during the campaign, contributing 10 %-15 % to the total iron oxide fraction. Magnetite can be found in sediments in the Erongo region of coastal Namibia (Lohmeier et al., 2021) but also in anthropogenic emissions, such as those from metal smelting (Rathod et al., 2020). Zhang et al. (2022) investigated the light-absorbing properties and single-particle composition from airborne measurements offshore central Africa during the ORACLES 2018 campaign, and attributed the presence of magnetite to the high-temperature conversion of hematite and/or goethite in biomass-burning plumes or to industrial or vehicular emissions, including from pyro-metallurgical processing in the Zambian Copperbelt. Pyrite (FeS) and Feoxalate complexes were also detected throughout the campaign, but their average contribution was extremely low, with the exceptions of 28-29 August 2017 (T10, approximately 19 %) and 11 September (T35–36, approximately 30 %).

Pyrite Ferrihydrite

3.4 Iron solubility

Figure 7 presents the time series of the fractional solubility for Al, Si, and Fe, as well as those of fluoride (F⁻) and MSA measured in the TSP fraction during the field campaign.

During P1 and P2, the fractional solubility was measurable and of the order of 2 %–8 % for Fe, 9 %–24 % for Al, 5 %–17 % for Si, and 1.5 %–4 % for Ti (not shown). After that, during P3, their fractional solubility drastically dropped to 0.2 %–1.7 % for Fe and 0.2 %–2.6 % for Al, whereas the fractional solubility of Si and Ti was not measurable (dissolved concentrations under limit of detection). A similar behaviour was observed for most of the measured trace metals (As, Co, Cr, Cu, Ni, Pb, Ti, and Zn, Fig. S9).

The percent fractional solubility of iron measured during P1 and P2 was of the same order of magnitude as the lowest solubility values reported at the same sampling site for PM_{10} dust particles by Desboeufs et al. (2024) for the period April to December 2017, when values as high as 20% were measured when MSA in the particle phase was most

concentrated. These authors attributed the enhanced solubility to processing (photo-reduction) of the dust by gas-phase dimethyl sulfide (DMS) emitted by the coastal Benguela upwelling. In the present dataset, this association cannot be made. Figure 7 shows that the MSA concentrations were of the same order of magnitude throughout the campaign and actually slightly more concentrated during P2 and P3, when, on the other hand, the Fe fractional solubility was the lowest. Soluble Fe was also not correlated with oxalate (Pearson correlation coefficient $r \sim 0.3$), another renown organic ligand (Paris and Desboeufs, 2013).

 7 ± 4

 16 ± 4

 4 ± 5

 8 ± 4

On the other hand, Fig. 7 shows that during P1 and P2, the temporal variability of the fractional solubility of Al, Si, and Fe closely followed that of the mass concentration of fluoride (correlation coefficients of 0.87, 0.85, and 0.81, respectively). Fluoride has been identified to be a good ligand of metals in aqueous solution, notably Fe(III) in comparison to Fe(II) (Connick et al., 1956; Bond and Hefter, 1980). The abundance of fluoride ions could act to facilitate the metal complexation on the particle surfaces, potentially promoting their release from the bulk oxide and dissolution at the solid/liquid interface (Arnesen, 1998; Tao et al., 2022). In particular, F⁻ may contribute to the disruption of the Si–O lattice bond by forming SiF₆²⁻ complexes at acidic pH (Mitra and Rimstidt, 2009).

4 Conclusive remarks

The 3 weeks of aerosol sampling at the Henties Bay coastal site in Namibia during the AEROCLO-sA field campaign coincided with a transition period between two synoptic regimes: the dominance of southerly air flow, associated with the reinforcement of the South Atlantic anticyclone (22 to 31 August 2017), and the dominance of north-easterly air flow (1 to 12 September 2017), associated with the installation of the mid-tropospheric continental high. These synoptic regimes corresponded to a significant change in the aerosol composition measured at the site and in particular of that of mineral dust. During August and the first few days of September, the dust was natural windblown from

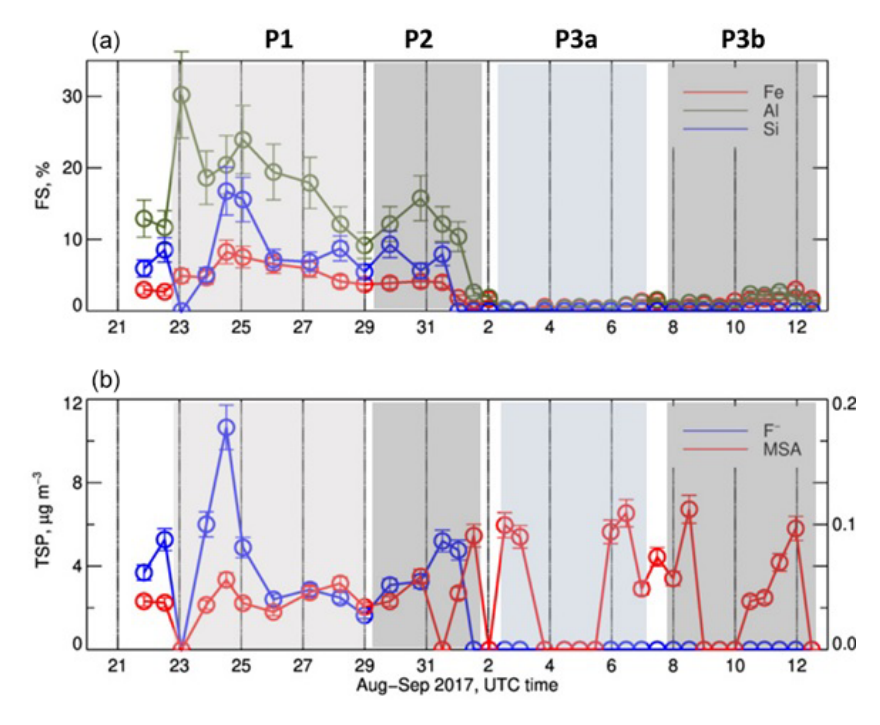


Figure 7. (a) Time series of the fractional solubility of Al, Si, and Fe in the TSP fraction. (b) Time series of concentrations of F⁻ (blue) and MSA (red) in the TSP fraction. The MSA concentrations are reported on the right axis of (b). Missing data correspond to periods when the measured concentrations were below the detection limit. Error bars on concentrations represent the analytical errors. Error bars on ratios represent the sum of percent analytical errors on measured concentrations.

the southerly gravel plains with a composition consistent with that previously found in Namibia (Klopper et al., 2020). Later, the dust was fugitive from anthropogenic mining and possibly also from smelting emissions as far as in the Zambian Copper Belt. The anthropogenic influence in the latter part of the campaign was also documented by the composition of the organic aerosol, which was rich in highly unsaturated compounds as well as saturated N-containing compounds in the latter two periods, more typical of anthropogenic pollution. A second major difference in the composition of the air masses was the high fluoride content until 2 September, attributed to emissions from the marine shelf south of Henties Bay.

Taking advantage of these differences, this paper presents the first case study analysis of differences and similarities in the composition of natural and anthropogenic dust, with two key findings: (1) the elemental composition of the anthropogenic dust is enriched in silicon and heavy metals, notably As, Mn, Cu, Cd, Pb, and Zn, and depleted in Al; (2) metals in anthropogenic dust are less water-soluble than in the natural aeolian dust. In particular, the fractional solubility of iron in the natural dust ranged between 2% and 8% but remained lower than 2% in the anthropogenic dust. This is rather unexpected when taking into account the current literature on anthropogenic dust being influenced by combustion, reporting that the iron solubility would be the order of 50% (e.g. Li et al., 2017; Ueda et al., 2023). There are various possible

explanations for this: first of all, the mineralogy of iron. The most soluble form, ferrihydrite (Journet et al., 2008; Shi et al., 2012), was slightly more abundant in the natural dust, while the less soluble forms of iron (iron oxides such as hematite and magnetite) were more frequent in the fugitive dust, which, conversely, could be more efficient in absorbing light at short wavelengths. Secondly, during the first part of the campaign, the aerosol particles were smaller in size, which is known to promote particle solubility, both directly and indirectly, allowing more intense atmospheric processing (Hamilton et al., 2022). Thirdly, our results indicate in a very clear way the extent of which the solubility of iron is linked to the abundance of fluoride ions during the first part of the campaign. While we do not have insights into the mineralogical forms of the metals other than iron, the similar behaviour of their dissolved concentrations, in particular Al and Si, suggests that the marine emissions of fluoride from the Benguela shelf could play a key role in sustaining the complexation of metals dust particles and facilitate their dissolution, supplementing the processing by DMS described for iron in Desboeufs et al. (2024). Such high concentrations of F⁻ ions not only are unexpected but also open questions for further studies in this environment. Similarly, regarding what is known for chloride or bromine (Finlayson-Pitts, 2010, Simpson et al., 2015), one cannot exclude recycling F⁻ into reactive fluorinated radicals through heterogeneous processes. This calls for further targeted reanalysis of the organic matter sampled during this campaign in both the gaseous and particulate phases and for further laboratory work to investigate this quite poorly known chemistry. Finally, our results suggest that, in the absence of processing by DMS or oceanic fluoride, the transport of mining dust, including from the Zambian Copper Belt, is unlikely to be a significant source of dissolved iron but also of elements such as Mn, Cu, and Zn, which are toxic to phytoplankton even at low concentrations and, if assimilated, could alter the oceanic productivity and microbial biogeochemistry (Adriano, 2001; Jordi et al., 2012; Mahowald et al., 2018; Yang et al. 2019).

Future work should expand these results by addressing the frequency and intensity of those occurrences on a longer timescale, as well as the mineralogy of metals and their processing by marine emissions in the laboratory.

Code availability. The FASTOSH XANES data analysis package is available for download at https://www.synchrotron-soleil.fr/fr/lignes-de-lumiere/samba (last access: 2 March 2024).

Data availability. All data are made freely available by the French national service for atmospheric data, AERIS, at https://pegasus.aeris-data.fr/catalogue/ (last access: 2 March 2025).

Supplement. The supplement related to this article is available online at https://doi.org/10.5194/acp-25-16127-2025-supplement.

Author contributions. PF coordinated the AEROCLO-sA project and funding, led the field campaign and the data analysis, and wrote the manuscript with contributions from all the co-authors. SM performed PMF analysis. AZ performed ESI-HRMS analysis and analysed data. CG collected samples and supervised PMF and ESI-HRMS analyses and their data interpretation. CB contributed to the interpretation of the dust solubility and composition. KD analysed the fractional solubility measurements. MG analysed CAMS reanalysis. GS performed back-trajectory calculations. SC performed XRF analysis, ST performed IC/ICP analysis, and FB and CDB performed XANES measurements under the supervision of GL. AF, JFD, AN, and SJP facilitated the field campaign and participated in it.

Competing interests. At least one of the (co-)authors is a member of the editorial board of *Atmospheric Chemistry and Physics*. The peer-review process was guided by an independent editor, and the authors also have no other competing interests to declare.

Disclaimer. Publisher's note: Copernicus Publications remains neutral with regard to jurisdictional claims made in the text, published maps, institutional affiliations, or any other geographical representation in this paper. While Copernicus Publications makes ev-

ery effort to include appropriate place names, the final responsibility lies with the authors.

Special issue statement. This article is part of the special issue "New observations and related modelling studies of the aerosol-cloud-climate system in the Southeast Atlantic and southern Africa regions (ACP/AMT inter-journal SI)". It is not associated with a conference.

Acknowledgements. Authors are grateful to the AEROCLO-sA consortium for their work in the field and during the preparation of the field campaign and SANUMARC for hosting the field campaign. The authors wish to thank AERIS (https://www.aeris-data. fr/, last access: 2 March 2025), the French atmospheric Data and Service Centre, for providing the campaign website and organizing the curation and open distribution of AEROCLO-sA data.

Financial support. This work was supported by the French National Research Agency under grant agreement no. ANR-15-CE01-0014-01, the French national program LEFE/INSU, the French National Agency for Space Studies (CNES), and the South African National Research Foundation (NRF) under grant UID 105958. Chiara Giorio's work was supported by the Supporting TAlent in ReSearch@University of Padova STARS-StG "MOCAA" and a BP Next Generation fellowship awarded by the Yusuf Hamied Department of Chemistry at the University of Cambridge. This research received additional resources through the "The role of Secondary Organic Aerosols on the climate over the west coast of southern Africa (SOA-Clim)", an international research project supported by the University of Cambridge and CNRS. Marco Gaetani was supported by the project "Dipartimento di Eccellenza 2023–2027", funded by the Italian Ministry of Education, University and Research at IUSS Pavia. The PEGASUS facility receives funding as a national facility (instrument national) of the CNRS INSU.

Review statement. This paper was edited by Lea Hildebrandt Ruiz and reviewed by Akinori Ito and one anonymous referee.

References

Adebiyi, A., Kok, J. F., Murray, B. J., Ryder, C. L., Stuut, J.-B. W., Kahn, R. A., Knippertz, P., Formenti, P., Mahowald, N. M., Pérez García-Pando, C., Klose, M., Ansmann, A., Samset, B. H., Ito, A., Balkanski, Y., Di Biagio, C., Romanias, M. N., Huang, Y., and Meng, J.: A review of coarse mineral dust in the Earth system, Aeol. Res., 60, 100849, https://doi.org/10.1016/j.aeolia.2022.100849, 2023.

Adriano, D. C.: Trace elements in terrestrial environments: biogeochemistry, bioavailability, and risks of metals, 2nd edn., New York Berlin Heidelberg, Springer, https://doi.org/10.1007/978-0-387-21510-5, 2001.

Anbar, M. and Neta, P.: Reaction of fluoride ions with hydrogen atoms in aqueous solution, T. Faraday Soc., 63, 141–146, https://doi.org/10.1039/tf9676300141, 1967.

- Arnesen, A. K. M.: Effect of fluoride pollution on pH and solubility of Al, Fe, Ca, Mg, K and organic matter in soil from Ardal (Western Norway), Water. Air Soil Poll., 103, 375–388, https://doi.org/10.1023/A:1004921600022, 1998.
- Atlas, E. and Pytkowicz, R. M.: Solubility behavior of apatites in seawater, Limnol. Oceanogr., 22, 290–300, https://doi.org/10.4319/lo.1977.22.2.0290, 1977.
- Aurélien, N., Ousmane, S. and Pitiya, R.: Zambia's Copperbelt Area and Copper Mining: A Review, J. Geosci. Environ. Protection, 10, 67–75, https://doi.org/10.4236/gep.2022.103005, 2022.
- Baldo, C., Formenti, P., Nowak, S., Chevaillier, S., Cazaunau, M., Pangui, E., Di Biagio, C., Doussin, J.-F., Ignatyev, K., Dagsson-Waldhauserova, P., Arnalds, O., MacKenzie, A. R., and Shi, Z.: Distinct chemical and mineralogical composition of Icelandic dust compared to northern African and Asian dust, Atmos. Chem. Phys., 20, 13521–13539, https://doi.org/10.5194/acp-20-13521-2020, 2020.
- Bikkina, P., Kawamura, K., Bikkina, S., Kunwar, B., Tanaka, K., and Suzuki, K.: Hydroxy Fatty Acids in Remote Marine Aerosols over the Pacific Ocean: Impact of Biological Activity and Wind Speed, ACS Earth and Space Chemistry, 3, 366–379, https://doi.org/10.1021/acsearthspacechem.8b00161, 2019.
- Bond, A. M. and Hefter, G. T. (Eds.): Critical Survey of Stability Constants and Related Thermodynamic Data of Fluoride Complexes in Aqueous Solution, Pergamon, ii, https://doi.org/10.1016/B978-0-08-022377-3.50001-6, 1980.
- Briois, V., Fonda, E., Belin, S., Barthe, L., La Fontaine, C., Langlois, F., Ribbens, M., and Villain, F.: SAMBA: The 4–40 keV X-ray absorption spectroscopy beamline at SOLEIL, UVX 2010 10e Colloque sur les Sources Cohérentes et Incohérentes UV, VUV et X, Applications et Développements Récents, EDP Sciences, Les Ulis, France, 41–47, https://doi.org/10.1051/uvx/2011006, 2011.
- Caponi, L., Formenti, P., Massabó, D., Di Biagio, C., Cazaunau, M., Pangui, E., Chevaillier, S., Landrot, G., Andreae, M. O., Kandler, K., Piketh, S., Saeed, T., Seibert, D., Williams, E., Balkanski, Y., Prati, P., and Doussin, J.-F.: Spectral- and size-resolved mass absorption efficiency of mineral dust aerosols in the shortwave spectrum: a simulation chamber study, Atmos. Chem. Phys., 17, 7175–7191, https://doi.org/10.5194/acp-17-7175-2017, 2017.
- Cavalli, F., Viana, M., Yttri, K. E., Genberg, J., and Putaud, J.-P.: Toward a standardised thermal-optical protocol for measuring atmospheric organic and elemental carbon: the EUSAAR protocol, Atmos. Meas. Tech., 3, 79–89, https://doi.org/10.5194/amt-3-79-2010, 2010.
- Chazette, P., Flamant, C., Totems, J., Gaetani, M., Smith, G., Baron, A., Landsheere, X., Desboeufs, K., Doussin, J.-F., and Formenti, P.: Evidence of the complexity of aerosol transport in the lower troposphere on the Namibian coast during AEROCLO-sA, Atmos. Chem. Phys., 19, 14979–15005, https://doi.org/10.5194/acp-19-14979-2019, 2019.
- Chen, S., Chen, J., Zhang, Y., Lin, J., Bi, H., Song, H., Chen, Y., Lian, L., Liu, C., and Zhang, R.: Anthropogenic dust: sources, characteristics and emissions, Environ. Res. Lett., 18, 103002, https://doi.org/10.1088/1748-9326/acf479, 2023.
- Compton, J. S. and Bergh, E. W.: Phosphorite deposits on the Namibian shelf, Mar. Geol., 380, 290–314, https://doi.org/10.1016/j.margeo.2016.04.006, 2016.

- Connick, R. E., Hepler, L. G., Hugus, Z. Z. Jr., Kury, J. W., Latimer, W. M., and Tsao, M.-S.: The Complexing of Iron(III) by Fluoride Ions in Aqueous Solution: Free Energies, Heats and Entropies, J. Am. Chem. Soc., 78, 1827–1829, https://doi.org/10.1021/ja01590a015, 1956.
- Dansie, A. P., Wiggs, G. F. S., and Thomas, D. S. G.: Iron and nutrient content of wind-erodible sediment in the ephemeral river valleys of Namibia, Geomorphology, 290, 335–346, https://doi.org/10.1016/j.geomorph.2017.03.016, 2017a.
- Dansie, A. P., Wiggs, G. F. S., Thomas, D. S. G., and Washington, R.: Measurements of windblown dust characteristics and ocean fertilization potential: The ephemeral river valleys of Namibia, Aeolian Research, 29, 30–41, https://doi.org/10.1016/j.aeolia.2017.08.002, 2017b.
- Dansie, A. P., Thomas, D. S. G., Wiggs, G. F. S., and Munkittrick, K. R.: Spatial variability of ocean fertilizing nutrients in the dust-emitting ephemeral river catchments of Namibia, Earth Surface Processes and Landforms, 43, 563–578, https://doi.org/10.1002/esp.4207, 2018.
- Dansie, A. P., Thomas, D. S. G., Wiggs, G. F. S., Baddock, M. C., and Ashpole, I.: Plumes and blooms Locally-sourced Ferich aeolian mineral dust drives phytoplankton growth off southwest Africa, Science of The Total Environment, 829, 154562, https://doi.org/10.1016/j.scitotenv.2022.154562, 2022.
- Desboeufs, K., Formenti, P., Torres-Sánchez, R., Schepanski, K., Chaboureau, J.-P., Andersen, H., Cermak, J., Feuerstein, S., Laurent, B., Klopper, D., Namwoonde, A., Cazaunau, M., Chevaillier, S., Feron, A., Mirande-Bret, C., Triquet, S., and Piketh, S. J.: Fractional solubility of iron in mineral dust aerosols over coastal Namibia: a link to marine biogenic emissions?, Atmos. Chem. Phys., 24, 1525–1541, https://doi.org/10.5194/acp-24-1525-2024, 2024.
- Eltayeb, M. A. H., Van Grieken, R. E., Maenhaut, W., and Annegarn, H. J.: Aerosol-soil fractionation for Namib Desert samples, Atmospheric Environment. Part A. General Topics, 27, 669–678, https://doi.org/10.1016/0960-1686(93)90185-2, 1993.
- Ettler, V., Mihaljevič, M., Kříbek, B., Majer, V., and Šebek, O.: Tracing the spatial distribution and mobility of metal/metalloid contaminants in Oxisols in the vicinity of the Nkana copper smelter, Copperbelt province, Zambia, Geoderma, 164, 73–84, https://doi.org/10.1016/j.geoderma.2011.05.014, 2011.
- Ettler, V., Vítková, M., Mihaljevič, M., Šebek, O., Klementová, M., Veselovský, F., Vybíral, P., and Kříbek, B.: Dust from Zambian smelters: mineralogy and contaminant bioaccessibility, Environ. Geochem. Hlth., 36, 919–933, https://doi.org/10.1007/s10653-014-9609-4, 2014.
- Finlayson-Pitts, B.: Halogens in the troposphere, Anal. Chem., 82, 770–776, https://doi.org/10.1021/ac901478p, 2010.
- Flamant, C., Gaetani, M., Chaboureau, J.-P., Chazette, P., Cuesta, J., Piketh, S. J., and Formenti, P.: Smoke in the river: an Aerosols, Radiation and Clouds in southern Africa (AEROCLO-sA) case study, Atmos. Chem. Phys., 22, 5701–5724, https://doi.org/10.5194/acp-22-5701-2022, 2022.
- Formenti, P., Nava, S., Prati, P., Chevaillier, S., Klaver, A., Lafon, S., Mazzei, F., Calzolai, G., and Chiari, M.: Self-attenuation artifacts and correction factors of light element measurements by X-ray analysis: Implication for mineral dust composition studies, J. Geophys. Res., 115, D01203, https://doi.org/10.1029/2009JD012701, 2010.

- Formenti, P., Caquineau, S., Chevaillier, S., Klaver, A., Desboeufs, K., Rajot, J. L., Belin, S., and Briois, V.: Dominance of goethite over hematite in iron oxides of mineral dust from Western Africa: quantitative partitioning by X-ray absorption spectroscopy, J. Geophys. Res., 119, 12740–1275, 2014.
- Formenti, P., Piketh, S. J., Namwoonde, A., Klopper, D., Burger, R., Cazaunau, M., Feron, A., Gaimoz, C., Broccardo, S., Walton, N., Desboeufs, K., Siour, G., Hanghome, M., Mafwila, S., Omoregie, E., Junkermann, W., and Maenhaut, W.: Three years of measurements of light-absorbing aerosols over coastal Namibia: seasonality, origin, and transport, Atmos. Chem. Phys., 18, 17003–17016, https://doi.org/10.5194/acp-18-17003-2018, 2018.
- Formenti, P., D'Anna, B., Flamant, C., Mallet, M., Piketh, S. J., Schepanski, K., Waquet, F., Auriol, F., Brogniez, G., Burnet, F., Chaboureau, J.-P., Chauvigné, A., Chazette, P., Denjean, C., Desboeufs, K., Doussin, J.-F., Elguindi, N., Feuerstein, S., Gaetani, M., Giorio, C., Klopper, D., Mallet, M. D., Nabat, P., Monod, A., Solmon, F., Namwoonde, A., Chikwililwa, C., Mushi, R., Welton, E. J. and Holben, B.: The Aerosols, Radiation and Clouds in Southern Africa Field Campaign in Namibia: Overview, Illustrative Observations, and Way Forward, B. Am. Meteorol. Soc., 100, 1277–1298, https://doi.org/10.1175/BAMS-D-17-0278.1, 2019.
- Frossard, A. A., Russell, L. M., Burrows, S. M., Elliott, S. M., Bates, T. S., and Quinn, P. K.: Sources and composition of submicron organic mass in marine aerosol particles, J. Geophys. Res, 119, 12977–13003, https://doi.org/10.1002/2014JD021913, 2014.
- Fuge, R.: Fluorine in the environment, a review of its sources and geochemistry, Appl. Geochem., 100, 393–406, https://doi.org/10.1016/j.apgeochem.2018.12.016, 2019.
- Gaetani, M., Pohl, B., Alvarez Castro, M. C., Flamant, C., and Formenti, P.: A weather regime characterisation of winter biomass aerosol transport from southern Africa, Atmos. Chem. Phys., 21, 16575–16591, https://doi.org/10.5194/acp-21-16575-2021, 2021.
- Gili, S., Vanderstraeten, A., Chaput, A., King, J., Gaiero, D. M., Delmonte, B., Vallelonga, P., Formenti, P., Di Biagio, C., Cazanau, M., Pangui, E., Doussin, J.-F., and Mattielli, N.: South African dust contribution to the high southern latitudes and East Antarctica during interglacial stages, Communications Earth & Environment, 3, 129, https://doi.org/10.1038/s43247-022-00464-z, 2022.
- Giorio, C., Doussin, J. F., D'Anna, B., Mas, S., Filippi, D., Denjean, C., Mallet, M. D., Bourrianne, T., Burnet, F., Cazaunau, M., Chikwililwa, C., Desboeufs, K., Feron, A., Michoud, V., Namwoonde, A., Andreae, M. O., Piketh, S. J., and Formenti, P.: Butene Emissions From Coastal Ecosystems May Contribute to New Particle Formation, Geophys. Res. Lett., 49, https://doi.org/10.1029/2022GL098770, 2022.
- Giorio, C., Monod, A., Di Marco, V., Herckes, P., Napolitano, D.,
 Sullivan, A., Landrot, G., Warnes, D., Nasti, M., D'Aronco, S.,
 Gérardin, A., Brun, N., Desboeufs, K., Triquet, S., Chevaillier,
 S., Di Biagio, C., Battaglia, F., Burnet, F., Piketh, S. J., Namwoonde, A., Doussin, J.-F., and Formenti, P.: Contrasting solubility and speciation of metal ions in total suspended particulate matter and fog from the coast of Namibia Part 1, Atmos. Chem.

- Phys., 25, 16107–16125, https://doi.org/10.5194/acp-25-16107-2025, 2025.
- Hamilton, D. S., Perron, M. M. G., Bond, T. C., Bowie, A. R., Buchholz, R. R., Guieu, C., Ito, A., Maenhaut, W., Myriokefalitakis, S., Olgun, N., Rathod, S. D., Schepanski, K., Tagliabue, A., Wagner, R., and Mahowald, N. M.: Earth, Wind, Fire, and Pollution: Aerosol Nutrient Sources and Impacts on Ocean Biogeochemistry, Annu. Rev. Mar. Sci., 14, 303–330, https://doi.org/10.1146/annurev-marine-031921-013612, 2022.
- Heine, K. and Völkel, J.: Clay Minerals in Namibia and their Significance for the Terrestrial and Marine Past Global Change Research, African Study Monographs, Supplementary Issue, 40, 31–50, The Research Committee for African Area Studies, Kyoto University, https://repository.kulib.kyoto-u.ac.jp/bitstream/2433/96299/1/ASM_S_40_31.pdf (last access: 2 March 2025), 2010.
- Hossein, M., Rwiza, M. J., Nyanza, E. C., Bakari, R., Ripanda, A., Nkrumah, S., Selemani, J. R., and Machunda, R. L.: Fluoride contamination a silent global water crisis: A Case of Africa, Scientific African, 26, e02485, https://doi.org/10.1016/j.sciaf.2024.e02485, 2024.
- Inness, A., Ades, M., Agustí-Panareda, A., Barré, J., Benedictow, A., Blechschmidt, A.-M., Dominguez, J. J., Engelen, R., Eskes, H., Flemming, J., Huijnen, V., Jones, L., Kipling, Z., Massart, S., Parrington, M., Peuch, V.-H., Razinger, M., Remy, S., Schulz, M., and Suttie, M.: The CAMS reanalysis of atmospheric composition, Atmos. Chem. Phys., 19, 3515–3556, https://doi.org/10.5194/acp-19-3515-2019, 2019.
- Jordi, A., Basterretxea, G., Tovar-Sánchez, A., Alastuey, A., and Querol, X.: Copper aerosols inhibit phytoplankton growth in the Mediterranean Sea, P. Nat. Acad. Sci. USA, 109, 21246–21249, https://doi.org/10.1073/pnas.1207567110, 2012.
- Journet, E., Desboeufs, K., Caquineau, S., and Colin, J. L.: Mineralogy as a critical factor of dust iron solubility, Geophys. Res. Lett., 35, https://doi.org/10.1029/2007GL031589, 2008.
- Klopper, D., Formenti, P., Namwoonde, A., Cazaunau, M., Chevaillier, S., Feron, A., Gaimoz, C., Hease, P., Lahmidi, F., Mirande-Bret, C., Triquet, S., Zeng, Z., and Piketh, S. J.: Chemical composition and source apportionment of atmospheric aerosols on the Namibian coast, Atmos. Chem. Phys., 20, 15811–15833, https://doi.org/10.5194/acp-20-15811-2020, 2020.
- Knippertz, P. and Stuut, J.-B. W: Mineral Dust: A Key Player in the Earth System, ed. Springer Dordrecht, https://doi.org/10.1007/978-94-017-8978-3, 2014.
- Kok, J. F., Storelvmo, T., Karydis, V. A., Adebiyi, A. A., Mahowald, N. M., Evan, A. T., He, C., and Leung, D. M.: Mineral dust aerosol impacts on global climate and climate change, Nature Reviews Earth & Environment, 4, 71–86, https://doi.org/10.1038/s43017-022-00379-5, 2023.
- Kříbek, B., Nyambe, I., Sracek, O., Mihaljevič, M., and Knésl, I.: Impact of Mining and Ore Processing on Soil, Drainage and Vegetation in the Zambian Copperbelt Mining Districts: A Review, Minerals, 13, 384, https://doi.org/10.3390/min13030384, 2023.
- Li, W., Xu, L., Liu, X., Zhang, J., Lin, Y., Yao, X., Gao, H., Zhang, D., Chen, J., Wang, W., Harrison, R. M., Zhang, X., Shao, L., Fu, P., Nenes, A., and Shi, Z.: Air pollution aerosol interactions produce more bioavailable iron for ocean ecosystems, Sci. Adv., 3, e1601749, https://doi.org/10.1126/sciadv.1601749, 2017.

- Liebenberg-Enslin, H., von Oertzen, D., and Mwananawa, N.: Dust and radon levels on the west coast of Namibia What did we learn?, Atmos. Poll. Res., 11, 2100–2109, https://doi.org/10.1016/j.apr.2020.05.020, 2020.
- Lohmeier, S., Lottermoser, B. G., Strauß, K., Adolffs, T., Sindern, S., and Gallhofer, D.: Nearshore marine garnet and magnetite placers in the Erongo and S-Kunene regions, Namibia, J. Afr. Earth Sci., 180, 104221, https://doi.org/10.1016/j.jafrearsci.2021.104221, 2021.
- Mahowald, N. M., Hamilton, D. S., Mackey, K. R. M., Moore, J. K., Baker, A. R., Scanza, R. A., and Zhang, Y.: Aerosol trace metal leaching and impacts on marine microorganisms, Nat. Commun., 5, 2614, https://doi.org/10.1038/s41467-018-04970-7, 2018.
- Mänd, K., Kirsimäe, K., Lepland, A., Crosby, C., Bailey, J., Konhauser, K., Wirth, R., Schreiber, A., and Lumiste, K.: Authigenesis of biomorphic apatite particles from Benguela upwelling zone sediments off Namibia: The role of organic matter in sedimentary apatite nucleation and growth, Geobiology, 16, https://doi.org/10.1111/gbi.12309, 2018.
- Martínez-Alonso, S., Veefkind, J. P., Dix, B., Gaubert, B., Theys, N., Granier, C., Soulié, A., Darras, S., Eskes, H., Tang, W., Worden, H., de Gouw, J., and Levelt, P. F.: S-5P/TROPOMI-derived NOx emissions from copper/cobalt mining and other industrial activities in the Copperbelt (Democratic Republic of Congo and Zambia), Geophys. Res. Lett., 50, e2023GL104109. https://doi.org/10.1029/2023GL104109, 2023.
- Meter, S. L., Formenti, P., Piketh, S. J., Annegarn, H. J., and Kneen, M. A.: PIXE investigation of aerosol composition in the Zambian Copperbelt, Nucl. Inst. Meth., B150, 433–438, 1999.
- Micella, I., Kroeze, C., Bak, M. P., and Strokal, M.: Causes of coastal waters pollution with nutrients, chemicals and plastics worldwide, Mar. Pollut. Bull., 198, 115902, https://doi.org/10.1016/j.marpolbul.2023.115902, 2024.
- Mileusnić, M., Mapani, B. S., Kamona, A. F., Ružičić, S., Mapaure, I., and Chimwamurombe, P. M.: Assessment of agricultural soil contamination by potentially toxic metals dispersed from improperly disposed tailings, Kombat mine, Namibia, J. Geochem. Explor., 144, 409–420, https://doi.org/10.1016/j.gexplo.2014.01.009, 2014.
- Mitra, A. and Rimstidt, J. D.: Solubility and dissolution rate of silica in acid fluoride solutions, Geochim. Cosmochim. Ac., 73, 7045–7059, https://doi.org/10.1016/j.gca.2009.08.027, 2009.
- Mwaanga, P., Silondwa, M., Kasali, G., and Banda, P. M.: Preliminary review of mine air pollution in Zambia, Heliyon, 5, e02485, https://doi.org/10.1016/j.heliyon.2019.e02485, 2019.
- Nekhoroshkov, P., Bezuidenhout, J., Zinicovscaia, I., Yushin, N., Vergel, K., and Frontasyeva, M.: Levels of Elements in Typical Mussels from the Southern Coast of Africa (Namibia, South Africa, Mozambique): Safety Aspect, Water, 13, 3238, https://doi.org/10.3390/w13223238, 2021.
- Nyanganyura, D., Maenhaut, W., Mathuthu, M., Makarau, A., and Meixner, F. X.: The chemical composition of tropospheric aerosols and their contributing sources to a continental background site in northern Zimbabwe from 1994 to 2000, Atmos. Environ., 41, 2644–2659, https://doi.org/10.1016/j.atmosenv.2006.11.015, 2007.
- O'Day, P. A., N. Rivera Jr., R. Root, and S. A. Carroll: X-ray absorption spectroscopic study of Fe reference compounds for

- the analysis of natural sediments, Am. Mineral., 89, 572–585, https://doi.org/10.2138/am-2004-0412, 2004.
- Omoregie, E., Vellemu, E. C., Nashima, F., Mudumbi Samona Brian, B., Liswaniso Gadaffi, G., and Shimooshili, K.: Assessment of copper levels along the Namibian marine coastline, GSC Biological and Pharmaceutical Sciences, 7, 48–55, https://doi.org/10.30574/gscbps.2019.7.3.0101, 2019.
- Onjefu, S. A., Shaningwa, F., Lusilao, J., Abah, J., Hess, E., and Kwaambwa, H. M.: Assessment of heavy metals pollution in sediment at the Omaruru River basin in Erongo region, Namibia, Environ. Poll. Bioavailability, 32, 187–193, 10.1080/26395940.2020.1842251, 2020.
- Onipe, T., Edokpayi, J. N., and Odiyo, J. O.: A review on the potential sources and health implications of fluoride in groundwater of Sub-Saharan Africa, J. Environ. Sci. Heal. A, 55, 1078–1093, https://doi.org/10.1080/10934529.2020.1770516, 2020.
- Paatero, P.: Least squares formulation of robust non-negative factor analysis, Chemometr. Intell. Lab., 37, 23–35, https://doi.org/10.1016/S0169-7439(96)00044-5, 1997.
- Paatero, P. and Tapper, U.: Positive matrix factorization: A non-negative factor model with optimal utilization of error estimates of data values, Environmetrics, 5, 111–126, https://doi.org/10.1002/env.3170050203, 1994
- Paris, R. and Desboeufs, K. V.: Effect of atmospheric organic complexation on iron-bearing dust solubility, Atmos. Chem. Phys., 13, 4895–4905, https://doi.org/10.5194/acp-13-4895-2013, 2013.
- Rakovan, J. F. and Hughes, J. M.: Strontium in the apatite structure: strontian fluorapatite and belovite-(ce), Can. Mineral., 38, 839– 845, https://doi.org/10.2113/gscanmin.38.4.839, 2000.
- Rajot, J.-L., Formenti, P., Alfaro, S., Desboeufs, K., Chevaillier, S., Chatenet, B., Gaudichet, A., Journet, E., Marticorena, B., Triquet, S., Maman, A., Mouget, N., and Zakou, A.: AMMA dust experiment: An overview of measurements performed during the dry season special observation period (SOP0) at the Banizoumbou (Niger) supersite, J. Geophys. Res., https://doi.org/10.1029/2008JD009906, 2008.
- Rathod, S. D., Hamilton, D. S., Mahowald, N. M., Klimont, Z., Corbett, J. J., and Bond, T. C.: A Mineralogy-Based Anthropogenic Combustion-Iron Emission Inventory, J. Geophys. Res., 125, e2019JD032114, https://doi.org/10.1029/2019JD032114, 2020.
- Seinfeld, J. H., and Pandis, S. N.: Atmospheric Chemistry and Physics: From Air Pollution to Climate Change, John Wiley and Sons, Inc., New York, 1326 pp., ISBN 9780471720188, 2006.
- Shi, Z., Krom, M. D., Jickells, T. D., Bonneville, S., Carslaw, K. S., Mihalopoulos, N., Baker, A. R., and Benning, L. G.: Impacts on iron solubility in the mineral dust by processes in the source region and the atmosphere: A review, Aeolian Research, 5, 21–42, https://doi.org/10.1016/j.aeolia.2012.03.001, 2012.
- Shikwambana, L. and Kganyago, M.: Meteorological Influence of Mineral Dust Distribution Over South-Western Africa Deserts Using Reanalysis and Satellite Data, Frontiers in Environmental Science, 10, https://doi.org/10.3389/fenvs.2022.856438, 2022.
- Simpson, W. R., Brown, S. S., Saiz-Lopez, A., Thornton, J. A., and von Glasow, R.: Tropospheric Halogen Chemistry: Sources, Cycling, and Impacts, Chem. Rev., 115, 4035–4062, https://doi.org/10.1021/cr5006638, 2015.
- Skamarock, W. C., Klemp, J. B., Dudhia, J., Gill, D. O., Barker, D., Duda, M. G., and Powers, J. G.: A Description

- of the Advanced Research WRF Version 3 (No. NCAR/TN-475+STR), University Corporation for Atmospheric Research, https://doi.org/10.5065/D68S4MVH, 2008.
- Sracek, O., Wanke, H., Ndakunda, N. N., Mihaljevič, M., and Buzek, F.: Geochemistry and fluoride levels of geothermal springs in Namibia, J. Geochem. Explor., 148, 96–104, https://doi.org/10.1016/j.gexplo.2014.08.012, 2015.
- Sracek, O.: Formation of secondary hematite and its role in attenuation of contaminants at mine tailings: review and comparison of sites in Zambia and Namibia, Front. Environ. Sci., 2, https://doi.org/10.3389/fenvs.2014.00064, 2015.
- Stein, A. F., Draxler, R. R., Rolph, G. D., Stunder, B. J. B., Cohen, M. D., and Ngan, F.: NOAA's HYSPLIT Atmospheric Transport and Dispersion Modeling System, Bulletin of the American Meteorological Society, 96, 2059–2077, https://doi.org/10.1175/BAMS-D-14-00110.1, 2015.
- Strain, E. M. A., Lai, R. W. S., White, C. A., Piarulli, S., Leung, K. M. Y., Airoldi, L., and O'Brien, A.: Editorial: Marine Pollution Emerging Issues and Challenges, Front. Mar. Sci., 9, 918984, https://doi.org/10.3389/fmars.2022.918984, 2022.
- Sylvanus, O., Kgabi, N., and Taole, S.: Heavy Metal Seasonal Distribution in Shore Sediment Samples along the Coastline of Erongo Region, Western Namibia, European Journal of Scientific Research, 139, 49–63, 2016.
- Tao, Y., Ye, G., Zhang, H., Hu, Y., Zuo, Q., Wang, X., Zhu, S., Kang, X., Zhang, Y., Xiang, X., Rong, Y., and Song, C.: Effect of Fluoride Ions on the Surface Dissolution of Vanadium-Bearing Biotite, Separations, 9, 422, https://doi.org/10.3390/separations9120422, 2022.
- Tournadre, J.: Anthropogenic pressure on the open ocean: The growth of ship traffic revealed by altimeter data analysis, Geophysical Research Letters, 41, 7924–7932, https://doi.org/10.1002/2014g1061786, 2014.
- Ueda, S., Iwamoto, Y., Taketani, F., Liu, M., and Matsui, H.: Morphological features and water solubility of iron in aged fine aerosol particles over the Indian Ocean, Atmos. Chem. Phys., 23, 10117–10135, https://doi.org/10.5194/acp-23-10117-2023, 2023.

- Usher, C. R., Michel, A. E., and Grassian, V. H.: Reactions on Mineral Dust, Chem. Rev., 103, 4883-4940, 10.1021/cr020657y, 2003.
- Vickery, K. J., Eckardt, F. D., and Bryant, R. G.: A sub-basin scale dust plume source frequency inventory for southern Africa, 2005–2008, Geophysical Research Letters, 40, 2013GL057321, https://doi.org/10.1002/grl.50968, 2013.
- von Holdt, J. R. and Eckardt, F. D.: Dust activity and surface sediment characteristics of the dustiest river in southern Africa: the Kuiseb River, Central Namib, South African Geographical Journal, 100, 104–121, https://doi.org/10.1080/03736245.2017.1339627, 2018.
- Yang, T., Chen, Y., Zhou, S., and Li, H.: Impacts of Aerosol Copper on Marine Phytoplankton: A Review, Atmosphere, 10, 414, https://doi.org/10.3390/atmos10070414, 2019.
- White, K., Walden, J., and Gurney, S. D.: Spectral properties, iron oxide content and provenance of Namib dune sands, Geomorphology, 86, 219–229, https://doi.org/10.1016/j.geomorph.2006.08.014, 2007.
- Wilke, M., Farges, F., Petit, P.-E., Brown, G. E. J., and Mertin, F.: Oxidation state and coordination of Fe in minerals: An Fe K-XANES spectroscopic study, Am. Mineral., 86, 714–730, https://doi.org/10.2138/am-2001-5-612 2001.
- Zhang, L., Segal-Rozenhaimer, M., Che, H., Dang, C., Sedlacek III, A. J., Lewis, E. R., Dobracki, A., Wong, J. P. S., Formenti, P., Howell, S. G., and Nenes, A.: Light absorption by brown carbon over the South-East Atlantic Ocean, Atmos. Chem. Phys., 22, 9199–9213, https://doi.org/10.5194/acp-22-9199-2022, 2022.
- Zherebker, A. O., Babcock, D. L., Pereira, S., D'Aronco, D., Filippi, L., Soldà, V., Michoud, A., Gratien, M., Cirtog, C., Cantrell, P., Formenti, and Giorio, C.: Decreasing the Uncertainty in the Comparison of Molecular Fingerprints of Organic Aerosols with H/D Exchange Mass Spectrometry, Environ. Sci. & Tech., 58, 20468–20479, https://doi.org/10.1021/acs.est.4c06749, 2024